1 2 9 0

UNIVERSIDADE Ð COIMBRA

Gonçalo Manuel Abrunhosa Coutinho

Tribological Behaviour of CoCrMo Alloys
Influence of Strain Hardening

Dissertação no âmbito do
Mestrado Integrado em Engenharia Mecânica

orientada por
Doutor Luís Miguel Cardoso Vilhena Pereira da Silva
e
Professor Doutor Amílcar Lopes Ramalho

apresentada no
Departamento de Engenharia Mecânica
Faculdade de Ciências e Tecnologia
Universidade de Coimbra

Outubro de 2021

Tribological Behaviour of CoCrMo Alloys
Influence of Strain Hardening
Análise da eficiência do endurecimento a frio no desgaste e propriedades mecânicas da liga Co28Cr6Mo

Dissertação apresentada para a obtenção do grau de Mestre em Engenharia Mecânica na Especialidade de Energia e Ambiente

Autor
Gonçalo Manuel Abrunhosa Coutinho

Orientadores
Doutor Luís Miguel Cardoso Vilhena Pereira da Silva, Investigador
Doutor Amílcar Lopes Ramalho, Prof. Catedrático

Júri

Presidente	**Doutor Diogo Mariano Simões Neto**
	Professor Auxiliar da Universidade de Coimbra
Orientador	**Doutor Luís Miguel Cardoso Vilhena Pereira da Silva**
	Investigador da Universidade de Coimbra
Vogal	**Doutor João Paulo da Silva Gil Nobre**
	Professor Auxiliar da Universidade de Coimbra

Coimbra, Outubro, 2021

AGRADECIMENTOS

Agradeço aos orientadores deste trabalho, Professor Doutor Amílcar Ramalho e Doutor Luís Vilhena a proposta do tema, a condução e o acompanhamento do desenvolvimento dos trabalhos, bem como todas as sugestões que foram permitindo o seu aperfeiçoamento ao longo de todo o semestre. Ao Professor Doutor Diogo Neto fico grato pelo apoio na modelação do problema a tratar. Dadas as dificuldades inerentes a um trabalho de investigação que tenta ir sempre ao encontro do desconhecido, ajudaram a traçar um novo trilho mais do que apenas seguir um já feito e bem conhecido.

Ao DEM/FCTUC pela disponibilização das instalações laboratoriais, indispensáveis ao trabalho experimental com o qual termino o meu percurso no Mestrado Integrado em Engenharia Mecânica da FCTUC.

RESUMO

O objectivo do presente trabalho de investigação foi o de determinar as condições ideais para as quais o endurecimento da superfície da liga Co28Cr6Mo conduz a melhores propriedades mecânicas. Uma vez que esta liga é utilizada em aplicações biomédicas sujeitas a elevadas solicitações mecânicas (por exemplo, articulações do joelho e da anca) e consequente elevado desgaste superficial das próteses, esta melhoria das suas propriedades mecânicas destina-se a prolongar a longevidade das suas aplicações no corpo humano, dilatando assim o tempo necessário entre intervenções cirúrgicas periódicas.

Os resultados mostram que o desgaste ocorrido numa superfície desta liga de Co28Cr6Mo está intimamente ligado à formação e fixação de óxidos nas marcas de desgaste. Sob determinadas condições de força normal aplicada durante o serviço (simulado através de testes tribológicos), ocorre esta formação de óxidos, que promove a criação de uma camada protetora contra o desgaste. As marcas associadas a testes tribológicos de provetes de Co28Cr6Mo endurecidos sob determinadas condições (de pressão normal, aplicada durante o endurecimento a frio) revelam uma elevada formação de óxidos e, paralelamente, um melhor comportamento mecânico, nomeadamente uma redução visível do volume de material removido quando sujeito ao desgaste. Assim, os resultados deste trabalho de investigação permitiram não só quantificar a influência dos óxidos na proteção desta liga contra o desgaste como concluir sobre quais seriam as condições ótimas de tratamento mecânico (endurecimento a frio) que estivessem associadas a este comportamento melhorado.

Palavras-chave: Co28Cr6Mo, Mechanical Test, Oxides, Coefficient of Friction, Wear, Tribological tests.

ABSTRACT

The objective of the present research work was to determine the optimal conditions that allow surface hardening of the Co28Cr6Mo alloy and consequently lead to increased mechanical properties. Since this alloy is used in biomedical applications that are subjected to high mechanical stresses (e.g. knee, shoulder and hip joints) and consequent high surface wear of the prostheses, this improvement of its mechanical properties is intended to extend the longevity of its applications in the human body, extending the time needed between periodic surgical interventions.

The results show that the wear occurring on a surface of this Co28Cr6Mo alloy is closely linked to the formation and attachment of oxides at the wear marks. Under certain conditions of normal force applied during service (simulated through tribological tests), this formation of oxides occurs, which promotes the creation of a protective layer against wear. The marks associated with tribological tests of Co28Cr6Mo specimens hardened under certain conditions (of normal pressure, applied during cold hardening) show a high formation of oxides and, in parallel, a better mechanical behaviour, namely a visible reduction of the volume of material removed when subjected to wear. Thus, the results of this research work allowed not only to quantify the influence of oxides in the protection of this alloy against wear, but also to conclude which would be the optimum conditions of mechanical treatment (cold hardening) that would be associated with this improved behaviour.

Keywords:	Co28Cr6Mo, Mechanical Test, Oxides, Coefficient of Friction, Wear, Tribological tests.

TABLE OF CONTENTS

LIST OF FIGURES

LIST OF TABLES

ACRONYMS

SEM - Scanning Electron Microscope

WC - Tungsten carbine

CoF - Coefficient of friction

1. INTRODUCTION

Cobalt-based alloys are materials whose cobalt-basis is alloyed with elements such as chromium, tungsten or nickel; they are composites whose major mass fraction is cobalt. The base combination of the majority of cobalt alloys is cobalt-chromium, with chromium acting as a strengthening alloy. Adding tungsten and/or molybdenum can improve strengthening even more. These alloys are typically used in challenging environments including high temperatures and acidic environments. Generally, cobalt-based alloys display pretty favourable mechanical properties. They are corrosion, wear and heat resistant and are therefore used for components in exigent applications, such as hot gas turbines or on the biomedical field. Cobalt also displays great resistance against sulphides, preventing any sulfidation of the material.

Metallic materials have been key materials to produce orthopaedic implants, due to their advantage in superior mechanical properties, including the high yield strength, ductility, fatigue strength and fracture toughness. Typically, the cobalt-chromium-molybdenum (CoCrMo) alloys are currently used for artificial joint replacement such as hip, knee, and shoulder prostheses (Wang and Xu, 2017). These alloys are conventionally produced via casting or forging route; however, additive manufacturing techniques have also recently been employed in their fabrication.

Among the cobalt chromium-based alloys, the Co28Cr6Mo (also known as ASTM F75, the Co28Cr6Mo cast alloy) has been by far the most applied alloy on the biomedical field over the last seven decades. This alloy shows a good combination of mechanical strength, fatigue and wear resistance, corrosion resistance and high biocompatibility. It possesses a good castability and hot workability, whilst the susceptibility to strain hardening makes difficult any kind of cold working (Vicente et al., 2011). When comparing to titanium alloys, also known for their good biocompatibility, the Co28Cr6Mo is more wear-resistant and is clinically used as bearing surfaces of the joint prostheses, such as artificial joint of metal-on-metal (MoM) bearings which were re-introduced by the early 1980s as an alternative to metal-on-polyethylene (MoP) bearings (Wang and Xu, 2017). However, we are still witnessing the emergence of new reports on periprosthetic tissue response to wear products generated by friction. This information encourages researchers to take measures to develop new materials, or methods to improve the properties of existing alloys (Mróz,

2017). The degradation of the implants during service life leads to the release into the body of toxic ions and wear particles. This continuous degradation is of concern for long-term stability of the implants. Published literature has highlighted the relevance of lubrication as well as metallurgical and contact mechanical factors on the degradation of CoCrMo implant alloys. Recent experimental investigations have proposed tribocorrosion, i.e., the interplay of mechanical wear and corrosion by the body fluids, as one of the crucial degradation mechanisms of implants (Mischler and Muñoz, 2013).

In the currently investigated Cobalt-based alloy, a big difference exists between the yield strength and the ultimate tensile strength; this means Co28Cr6Mo has high hardening potential. Therefore, this study aims the characterization in terms of hardening, friction, and wear of the Co28Cr6Mo (ASTM F75) alloy. It represents an opportunity to investigate if the previous superficial hardening of this Cobalt-based alloy affects its wear behaviour when in service and therefore can be a valid strengthening mechanism to increase implants' longevity on the human body.

The determination of cold-work conditions were performed and their respective impact on the mechanical properties of this Cobalt alloy were analysed. This work aims to verify whether the hardening was efficient (and what are the optimal conditions to obtain the best mechanical properties), to quantify not only the evolution of radial hardness in hardened samples but also the influence of surface hardening on the amount of material removed and its evolution with the force applied to the samples. In case of finding the approximately optimal cold-hardening conditions for this alloy, this research aims consequently to justify and validate them through different types of analysis.

2. LITERATURE REVIEW

Over the past decades, surgical implants have aimed at restoring the function of parts of the human body, prolonging life quality and expectancy. Biomaterials have had increasing use in the biomedical field (Zhou ZR et al., 2015) (Rampratap GK et al., 2015). Appropriate selection of materials is a key element to express the longevity of implants in the human body. The Co28Cr6Mo alloy owes its popularity in orthopaedics to the fact that it shows to have the best wear resistance compared to other currently used biomaterials (Pourzal R., Catelas I. et al, 2011). However, we are still witnessing the emergence of new reports on periprosthetic tissue response to wear products generated by friction. This information encourages researchers to implement measures in order to develop new materials, or methods to improve the mechanical properties of existing alloys (Mróz, 2017). Ideal implant property requirement is essentially summarised and categorised into three important features. The material must (a) be biocompatible, (b) possess required balance in mechanical and physical properties, and (c) be easy to fabricate, that is, be consistent with the natural geometry and be reproducible (Vilhena et al., 2019). Few published literature have revealed an important influence of previous strengthening mechanisms and treatments on microstructural and mechanical properties of CoCrMo alloys used on biomedical applications. There is a lot of investigation not only about this alloy's properties themself but also about its tribocorrosion behaviour.

Mori et al. (2012) found that the mechanical properties of a CoCrMo alloy (in this case Co29Cr6Mo0.14N) after hot rolling indicate an extremely high yield stress, which is more than twice the value observed prior to hot rolling. No dramatic reduction in elongation from the strength increase was detected, which demonstrates that hot rolling is effective for improving the strength–ductility balance of this alloy family. In that research, the increased strength caused by dislocation strengthening and by grain refinement was assessed quantitatively; the results demonstrate that dislocation strengthening makes a large contribution to the increase in the strength of the hot-rolled material.

Mróz (2017) studied the effect of manufacturing technology of ball-and-socket joints made of Co28Cr6Mo alloy on its tribological properties. Conclusions show that the ball-and-socket joints made from Co28Cr6Mo alloy, using the techniques of selective laser melting and spark plasma sintering are characterized by inferior tribological properties in

comparison with the reference material produced from ASTM F1537 LC. Plus, the study revealed that regardless of the production technology, the dominant type of wear of the friction surfaces was abrasive-adhesive wear. This investigation also showed poorer tribological wear resistance of the ball-and-socket joints produced by means of SLM (Selective Laser Melting) and SPS (Spark Plasma Sintering) technologies compared to the reference material.

Seki et al. (2019) investigated the effect of heat treatment on the microstructure and fatigue strength of CoCrMo alloys fabricated by selective laser melting. It was concluded that the heat-treated groups showed significantly higher fatigue lifetimes than the as-built groups. The heat treatment significantly improved fatigue strength due to the related microstructural changes. As-built CoCrMo alloys typically have specific columnar grains along the build direction; however, in that research, the heat-treated specimens contained equiaxed grains with random texture. Therefore, they proposed that thermally induced recrystallization resulted in residual stress relief and a subsequent increase in fatigue strength.

Reséndiz-Calderón et al. (2020) revealed new data about coefficient of friction behaviour and wear rates of boriding CoCrMo ASTM F1537 alloy under rolling and grooving micro-abrasion modes. It has been shown that wear resistance of the CoCrMo alloy was considerably increased after boriding, with a reduction in wear rate compared to the untreated alloy between 20% and 55% for grooving abrasion and between 6% and 10% for rolling abrasion. Moreover, the coefficient of friction of borided alloy revealed higher values when compared to the untreated alloy under rolling abrasion while a reduced coefficient of friction was found for the boriding alloy under grooving abrasion.

Mischler and Muñoz (2013) evaluated published results on the degradation of CoCrMo alloys using existing tribocorrosion concepts. Results showed that wear accelerated corrosion due to mechanical removal of the passive film during sliding is a major contribution to the overall degradation. Further, a transition from low to high wear coefficients was found at a threshold electrode potential close to 0.2 VSHE. These findings clearly showed that electrochemical phenomena play a key role in the tribological behaviour of biomedical CoCrMo alloy implants.

Balagna et al. (2012) characterized CoCrMo alloys after thermal treatment for high wear resistance. In this study, five alloys were used as substrates for a coating deposition by a thermal treatment in molten salts, in order to form a tantalum-rich coating on the

sample surface, able to improve the biocompatibility and wear resistance of the materials. The aim of that investigation was to evaluate the temperature effects on the structure, microstructure, mechanical and tribological properties of the considered substrates, after the removal of the coating by polishing. It was noticeable that the substrate crystalline structure changed during the heat treatment, inducing the formation of the hexagonal cobalt phase and the decrement of the cubic one. This crystallographic modification did not seem to influence the tribological behaviour of the substrates. On the contrary, it affected their strength and ductility. In conclusion, the properties of the CoCrMo alloys were affected by the tested thermal treatment in molten salts.

Chen et al. (2017) studied the effects of carbon addition on wear mechanisms of CoCrMo metal-on-metal hip joint bearings. This research showed that increasing the carbon content changes the microstructure of CoCrMo alloys, as it causes a higher degree of precipitation of globular carbides, which decreases the extent of wear. It was clear that high-carbon combinations exhibited excellent wear resistance. Abrasion was the dominant wear mechanism in the case of the low-carbon alloy, while surface fatigue caused by torn-off Mo-rich carbides was the dominant wear mechanism in the case of the high-carbon alloy. Further, in contrast to the Mo-rich carbides, the Cr-rich carbides limit three-body abrasion and increase the wear resistance.

Li et al. (2020) investigated the evolution of microstructures and their influence on the tribological properties of CoCrMo alloys processed by selective laser melting and subjected to heat treatment. This study proved the dense sub-grain boundaries and fine cellular dendrite decorated by microsegregation have a profound hardening effect on the selective laser melted and subsequently aged alloy. Plus, it showed that aging at high temperature (1150 ºC) induces homogenized recrystallization microstructure free of residual stress, which sharply decreased material nanohardness and scratch resistance.

Razavi et al. (2021) studied the effect of heat treatment on fatigue behaviour of as-built notched CoCrMo parts produced by Selective Laser Melting. Results showed both vacuum HT (heat treatment) and HIP (Hot Isostatic Pressing) had effects on the microstructure and internal defects, which resulted in an enhancement of fatigue properties. Performing heat treatment at 1150 °C in vacuum and HIP at 1150 °C and 1020 bar resulted in the reduction of internal porosity in the Selective Laser Melted specimens. Additionally, a ductility increase of 347% and 329% was observed for the Selective Laser Melted specimens subjected to HT and HIP, respectively. The presence of residual stresses together

with a high number of internal defects resulted in very poor fatigue behaviour of as-built SLM parts. This aspect was also significantly improved in the post treated parts, showing fatigue strength improvements of 180%, 136% for smooth specimens, 153% and 135% for notched specimens for HT and HIP conditions, respectively.

Ryu and Shrotriya (2013) evaluated the influence of roughness on surface instability of medical grade cobalt–chromium alloy (CoCrMo) during contact corrosion–fatigue. The experimental measurements of roughness changes after cyclic normal contacts and microetching of milled surface described the continuous motion of decrease and increase of roughness amplitudes due to stress-assisted dissolutions. The required thermodynamic properties were approximated and employed to identify surface characteristics in corrosion. In summary, a new approach of contact fatigue and corrosion was conducted to identify the influence of roughness condition and contact pressures on the early stage of contact corrosion–fatigue damage mechanism. As a result, the predictive equation of roughness instability enabled the authors to characterize the surface damage of rough surfaces during contact corrosion–fatigue.

Zai et al. (2019) aimed at the improvement of wear and corrosion resistance of the CoCrMo-UHMWPE (ultrahigh-molecular-weight polyethylene) pair articulating surfaces in the presence of an electrolyte. This study showed that the wear resistance of UHMWPE was improved by addition of multi-layer graphene to the polymer matrix, with graphene acting as a source of lubricant. Plus, the corrosion resistance of CoCrMo was improved by a sol-gel ZrO_2 coating sintered at a suitable temperature; this yielded an adherent coating which was thicker than the native oxide on bare CoCrMo and was also more resistant to abrasive wear. Furthermore, it became clear that the corrosion resistance under wear for the best modified pair is about 19.5 times higher than for the untreated pair.

García et al. (2010) described the tribological and wear resistance improvements of CoCrMo alloys implanted by Plasma Immersion (PI); friction and wear tests were performed to investigate the modifications obtained by oxygen implantation. Ultra micro-hardness tests revealed an increase of more than 80% in the hardness for the first nanometers in the implanted samples. Additionally, the friction coefficient obtained for the implanted samples was reduced from 0.36 for the untreated sample to below 0.1 at 520 and 540 °C. This paper also revealed important decreases in wear rate of close to a factor 10 for the implanted sample at high temperature (610 °C).

Henriques et al. (2015) investigated the influence of the processing conditions

on the mechanical properties of hot-pressed compacts of a CoCrMo biomedical alloy. The properties of the CoCrMo compacts showed to be significantly affected by the processing conditions, namely the temperature and time. Plus, the hot-pressing temperatures of 1000 °C and 1100 °C showed results in compacts with similar mechanical strength, porosity and Young's moduli. However, higher hardness values were registered for 1000 °C compacts when compared to those hot pressed at 1100 °C. The 900 °C compacts exhibited brittle behaviour while 1000 °C and 1100 °C compacts exhibited increasing ductility with increasing hot pressing temperature. This investigation has shown that hot pressing is an achievable technique for the production of CoCrMo compacts for biomedical applications with adequate mechanical properties; mechanical strength, porosity, Young's moduli and hardness can be adjusted by tuning the processing conditions.

Zhang et al. (2018) investigated the martensitic transformation and precipitation of CoCrMo alloys fabricated by selective laser melting (SLM) under aging heat treatment. They concluded that the rate increase of microhardness is related to the temperature and aging time. The long aging time and high aging temperature promoted the martensitic transformation and precipitation, which enhanced the microhardness. Specimens with highest microhardness were obtained by aging at 900 ºC for 10 hours.

Sadiq et al. (2015) characterised wear–corrosion or bio-tribocorrosion regimes of a CoCrMo alloy over a range of applied loads and applied potentials. The effects of applied potential and applied loads were investigated for a CoCrMo alloy in a physiological solution and in the presence of abrasive particles. This study showed that in the presence of abrasive particles wear–corrosion synergy is enhanced at low applied loading in comparison to the same test conditions in the absence of particles. Also, the results indicated that proteins present in foetal calf serum solution (the physiological solution) may result in the development of a graphitic tribo-layer, and play a critical role in enhancing or protecting against tribo-corrosive degradation.

Henriques et al. (2014) evaluated the mechanical and thermal properties of hot pressed CoCrMo–porcelain composites developed for prosthetic dentistry. The results of the study showed that CoCrMo particles exhibit good adhesion to the porcelain matrix. Additionally, the incorporation of metallic particles in the ceramic matrix increased the fracture strength (shear and flexural) of the composite and the presence of porcelain (ceramic phase) in the CoCrMo matrix showed to decrease it. It was also revealed that the coefficient of thermal expansion of metal–ceramic composites increases and hardness decreases

with increasing metallic particles content (although this increase is not linearly proportional to the composition).

Herranz et al. (2020) made a mechanical performance, corrosion and tribological evaluation of a low carbon CoCrMo alloy (more precisely, Co28Cr6Mo) processed by Metal Injection Moulding (MIM) for biomedical applications. This study allowed the authors to confirm that the low-carbon cobalt alloy processed by MIM exhibits an adequate equilibrium between its mechanical and corrosion behaviour, with a notable performance during fatigue and wear tests. The results confirmed the feasibility of CoCrMo alloys for biomedical uses and proved that MIM technology is an appropriate processing method for these materials.

Silva-Álvarez et al. (2020) improved the surface integrity of a CoCrMo alloy by the ball burnishing technique. They concluded that the burnishing force is the key factor in modifying the surface hardness, the roughness and the corrosion resistance, accounting for a contribution of 88.5%, 72.7% and 85.9%, respectively; after burnishing, the hardness increased from 416.5 HV to 584.5 HV, the surface roughness decreased from 0.1495 m to 0.0408 m and the corrosion rate changed from 636.04 mm/yr to 48.60 mm/yr. Summarizing, the ball burnishing process applied to the CoCrMo ally generated a refined surface layer that improves hardness, roughness and corrosion resistance.

Fleming et al. (2020) characterized the effect of melt temperature on the physical properties and chemical composition of investment cast ASTM F75 CoCrMo alloy. They found that increasing the melt temperature had the effect of removing nitrogen from the melt and adding oxygen. It was also determined that there was a strong positive correlation between nitrogen content and strength values. If desired, there is scope to minimise both oxygen pickup and nitrogen loss, nitrogen is correlated to increased mechanical properties of this alloy system by targeting lower melt temperatures.

Dorner-Reisel et al. (2004) studied the electrochemical corrosion behaviour of uncoated and Diamond-Like Carbon (DLC) coated Co28Cr6Mo alloy samples. They concluded that DLC coatings provide an useful measure for reducing the corrosion attack: the coatings' thickness is an essential factor for determining the extent of electrochemical corrosion. The authors stated that in addition to the two proven coating thickness of 0.8 mm and 2.7 mm, further coating thickness should be systematically investigated.

Vilhena et al. (2019) investigated the tribocorrosion of different biomaterials under reciprocating sliding conditions in artificial saliva. In this research, comparative ex-

periments were performed using commercial pure titanium (cP-Ti), Ti6Al4V alloy, pure niobium (Nb), and a Co28Cr6Mo alloy sliding against a Zirconia counterbody tested in artificial saliva. It was noticeable the wear volume increased monotonically with the increase in sliding distance times the normal load for all the four different test specimens. Furthermore, the Nb specimen showed a steady state coefficient of friction of the order of 1.13, much higher than those of the other three specimens, as follows: 0.60, 0.45, and 0.31 for respectively, cP-Ti, Ti6Al4V, and Co28Cr6Mo; the wear volume showed exactly the same tendency that was observed for the steady state coefficient of friction, as follows: Nb > cP-Ti > Ti6Al4V > Co28Cr6Mo. Additionally, all specimens showed a relationship between wear resistance, coefficient of friction, and hardness since the wear resistance depends on the material capacity to resist removal of material by abrasive particles and the wear mechanism was, predominantly, abrasive wear, while in Nb specimen, some points of adhesion were observed.

Patel et al. (2012) investigated Co28Cr6Mo ASTM F75 and ASTM F1537 conventionally manufactured Cobalt-based orthopaedic alloys and a spark plasma sintered (SPS) alloy and the relationship between their forming route, microstructure and tribological performance. In this study, the microstructure and phase analyses of the three alloys have been studied in detail and indicated that the two conventionally manufactured alloys show similar microstructures and phases; however, the SPS alloy had a very different microstructure and phase content. The phases within the microstructure determine the hardness of the alloy and the similar phases of the F75 and F1537 give similar microhardness, with the F75 being slightly higher due to the increased quantity of carbon enabling more carbides to be formed. The SPS alloy was much harder, due to the specific phases, such as the Hexagonal Closed Packed (HCP) Co, which has few slip systems and the rich phases of Cr, Mo and Cr_2O_3 that act as dislocation movement preventers, with the oxide being the hardest phase, making the alloy even harder. The nanohardness was higher than the microhardness due to formation of passive films that these CoCrMo alloys usually form on the surface of the alloy. The tribological performance of the three alloys was tested and it could be observed that the SPS alloy has 5–10 times lower wear rate compared to the other two alloys. Additionally, the metallic elemental content indicated that the SPS alloy releases much less Cr and Mo compared to the F75 and F1537, but still has a relatively high Co release. Overall, the SPS alloy showed an improvement in terms of tribological performance compared to the other conventionally fabricated alloys and released smaller

amounts of the Cr and Mo. Thus, in this research, this material showed significant promise as an alternative route for production of cobalt-based (Co28Cr6Mo) orthopaedic alloys.

Díaz et al. (2014) evaluated the reduction of corrosion current of CoCr alloys by post-PIII (Plasma Immersion Ion Implantation) oxidation. It was shown that post-oxidation by PIII leads to a more favourable corrosion protection with lower corrosion current and more positive corrosion potential compared to thermal oxidation or plasma oxidation. This study revealed PIII is the best alternative for forming a small surface modification of oxygen into CoCr alloys. It could be directly used for applications for biomaterials.

Mróz (2016) investigated the effect of manufacturing technology on the tribological properties of the ASTM F75 Co28Cr6Mo alloy. This researcher concluded that the samples prepared from this cobalt alloy using the technology of selective laser melting and spark plasma sintering are characterized by inferior tribological properties compared to the used reference material (ASTM F1537 LC). Furthermore, regardless of the production technology, the dominant type of wear of the friction surfaces was abrasive-adhesive.

Tonelli et al. (2020) studied the Co28Cr6Mo alloy processing by Selective Laser Melting (SLM), analysing the effect of Laser Energy Density (LED) on microstructure, surface morphology, and hardness. In this research, low LED was not sufficient enough to fully melt the feedstock powders; in account of extensive lacks of fusion, SLM samples exhibited a porosity content in the range 1–7%, high roughness on the top surface (Ra = 13−7 μm) and also a considerable variability in the macrohardness. On the other side, medium and high LED succeeded in melting all powders and returned sound components, with a very low porosity content (0.5–0.1 %) and smother top surfaces (Ra = 5-2.5 μm); in addition, hardness values had a very low variability. Dominant defects were micro-sized gas porosities although, if the energy density was too high (LED > 200 J mm^{-3}), key-hole collapses would occur. The energy density seemed to have no direct effect on the quality of lateral surfaces of samples and on the laser tracks size, both on the transverse and longitudinal sections. Plus, at a micro-level scale, the microstructure of all samples exhibited similar features: cellular grains with epitaxial growth crossing over layers, oriented along the direction of the maximum heat gradient.

Clemow and Daniell (1980) studied the influence of microstructure on the adhesive wear resistance of a CoCrMo alloy. The factors responsible for the difference in wear behaviour between three microstructural conditions of CoCrMo alloy were determined. This difference has been shown to be independent of the hardness of the face and is

known to reduce the adhesion of oxide scale on CoCr alloys. Therefore its formation on the surfaces of sliding pins could be expected to influence the transition load since this was dependent on oxide adhesion. Since similar experimental conditions were used for all tests in this research, such variables as interfacial temperature, atmosphere and bulk concentrations remained constant. In this case the presence of Cr_2O_3 on the surfaces of the solution treated pins could be attributed only to differences in the chromium concentration across the microstructure between the different conditions. Chromium is known to be fundamental in determining the formation of Cr_2O_3 in Co-C%, Ni-Cr and Fe-Cr alloys, and as a result of coring varied in concentration in the as-cast CoCrMO alloy specimens from 19% to 35% between the dendritic and interdendritic regions. The other main alloying element present, i.e. molybdenum, varied in the matrix only between 4% and 6%.

Liao et al. (2013) intended to outline some recent progresses in understanding wear and corrosion of metal-on-metal CoCrMo hip replacement both in-vivo and in-vitro. They concluded that the clinical outcomes of MoM hip replacements are variable: some MoM hip replacements have shown excellent performance for over 20 years, while some MoM devices failed a few years after implantation due to loosening or adverse local tissue reactions. The authors also stated that, in addition, a thorough understanding of the phase transformation of CoCrMo alloys is needed, as has been done for steels and many other alloys used in manufacturing. On the other side, it was noticeable that recent tribocorrosion studies of metal bearing have provided rich insight into the stimulated metal degradation with simultaneous wear and corrosion reactions. However, while the dependence of tribocorrosion on the applied load has been studied to some extent, the influence of the microstructure, e.g. grain size, second phases and chemical segregation to grain boundaries, on the tribocorrosion process is little understood.

Yoneyama et al. (2020) investigated the influence of Bovine Serum Albumin (BSA) on the tribocorrosion behaviour of a low carbon CoCrMo alloy in simulated body fluids. This study has shown that under its experimental conditions Albumin does not affect the passivation kinetics of the CoCrMo alloy, reduces wear and friction and increases the viscosity of the solution (and therefore enhances hydrodynamic effects which is the main mechanism by which albumin lowers wear). Moreover, albumin lowered the coefficient of friction below a threshold of approximately 0.22, but only under specific electrochemical conditions. As a consequence, the surface shear stress decreased and this limited the extent of mechanical mixing of oxide and metal and thus reduced wear.

Casabán Julián and Igual Muñoz (2011) evaluated the influence of microstructure of High Carbon (HC) CoCrMo biomedical alloys on the corrosion and wear behaviour in simulated body fluids. In this study, thermal treatments influenced the corrosion behaviour, passive dissolution and tribological response. Plus, an increase of grain boundaries accelerated the anodic reaction in all solutions. A higher carbide volume fraction generated a lower wear-rate. Microscopic observation by means of Optical and SEM microscopy showed that presence of proteins modified the debris behaviour. In nonprotein containing solutions particles were dispersed away from the track while in protein solutions particles tended to agglomerate and sediment around the wear track.

Sun et al. (2009) investigated the sliding-corrosion and abrasion-corrosion performance of a cast CoCrMo alloy in simulated hip joint environments using a microabrasion rig integrated with an electrochemical cell. Experimental results revealed that under abrasion-corrosion test conditions, the presence of proteins increased the total specific wear rate. Additionally, electrochemical noise measurements indicated that the average anodic current levels were appreciably lower for the proteinaceous solutions when compared with the inorganic solutions. A severely deformed nanocrystalline layer was identified immediately below the worn surface for both proteinaceous and inorganic solutions. The layer was formed by a recrystallisation process and/or a strain-induced phase transformation that occurs during microabrasion–corrosion.

Toh et al. (2017) reviewed the tribochemical characterization and tribocorrosion behaviour of CoCrMo alloys in which some remarks have been drawn. The authors affirmed that various tribochemical methods are, in general, employed to effectively characterize the tribocorrosive behaviour of CoCrMo alloys. Additionally, it was stated that long-term performance of CoCrMo alloys largely depends on the applied environmental conditions. Carbides play a pivotal role in the strengthening of CoCrMo alloys but also introduce unfavourable tribocorrosion conditions that are detrimental to the materials when dislodged from the matrices. In general, low-carbon CoCrMo alloys show a better wear resistance than high-carbon CoCrMo alloys. Also, alloying elements, such as Nitrogen, can be added to strengthen the alloys through the formation of nanograins and the use of carbon as a strengthener in CoCrMo alloys is perhaps restricted.

Mathew et al., (2011) compared two testing systems to evaluate the tribocorrosion behaviour of CoCrMo alloy for hip prosthesis as a function of loads. In the first configuration, "System A", a linearly reciprocating alumina ball slid against the flat metal im-

mersed in a phosphate buffer solution (PBS). In the second configuration, "System B", the flat end of a cylindrical metal pin was pressed against an alumina ball that oscillated rotationally, using bovine calf serum (BCS) as the lubricant and electrolyte. The tribocorrosion behaviour of the CoCrMo alloy was influenced by the test system; It was more favourable in System B, which was closer to in vivo conditions. Comparing System B against System A: the electrochemical impedance after sliding increased, whereas it decreased in System A; the polarization resistance increased, rather than decreased as in System A, indicating a protective effect and the wear factor and energy dissipation per unit mass loss were over an order of magnitude lower in System B than A. Additionally, except at the normal highest load, the dominant mass loss mechanism was wear-corrosion, suggesting marked synergism between wear and corrosion. The results for System B suggested that the dominant mass loss mechanism in metal-on-metal bearings is wear-corrosion. The notable differences between the two systems indicated that emulating key aspects of the in vivo conditions is important.

Yan et al. (2006) investigated tribocorrosion in implants, assessing high carbon (HC) and low carbon (LC) CoCrMo alloys by in situ electrochemical measurements. Tests were carried out in three different biological solutions: 50% calf bovine serum, Dulbecco's Modified Eagle's Medium (DMEM) and 0.36% NaCl solution at 37 °C with the specific objective being to attempt to isolate the effects of proteins and amino acid species in wear–corrosion. It was concluded that the interaction between tribological and electrochemical responses could be assessed by in situ electrochemical measurements and application of in situ monitoring had shown that corrosion plays a significant role in the overall degradation process in the various simulated biological fluids studied there. From a tribology point of view, comparing the three different fluids, proteins in 50% serum are believed to act as a lubricant and reduce friction. However, due to their effect on corrosion and tribocorrosion processes, they could enhance material degradation. Finally, among the materials that have been tested in this study, HC CoCrMo gave the lowest friction in simulated biological fluids and the lowest material loss, compared with LC CoCrMo. This was primarily because of its high corrosion resistance in tribocorrosion conditions.

2.1. Hertzian Contact Theory

It is important to introduce the Hertzian Contact Theory since the contact between crossed cylinders (between the Co28Cr6Mo samples and the respective counterbodies) can be described by it.

Stachowiak and Batchelor (2013) described the Hertzian Contact Theory. It is known that two contacting surfaces under a determined force will deform; the deformation may be either plastic or elastic depending on the material's properties and the magnitude of the applied force. In many engineering applications, for example, rolling contact bearings and gears, the contacting surfaces are non-conformal hence the resulting contact areas are very small and the resulting pressures are therefore very high. These stresses can be determined from the analytical formulae, based on the theory of elasticity, developed by Hertz in 1881.

Hertz's model of contact stress is based on the following assumptions, summarized by Stachowiak and Batchelor (2013), the authors of Engineering Tribology:

- the materials in contact are homogeneous and the yield stress is not exceeded;
- contact stress is caused by the load (normal to the contact tangent plane), which means that there are no tangential forces acting between the bodies;
- the contact area is very small compared with the dimensions of the contacting solids;
- the contacting solids are at rest and in equilibrium;
- the effect of surface roughness is negligible.

The evaluation of contact parameters is essential in many practical engineering applications. The most frequently used contact parameters, as stated by Stachowiak and Batchelor (2013), are:

- the contact area dimensions;
- the maximum contact pressure (often named Hertzian stress);
- the maximum deflection at the centre of the contacting surfaces;
- the position of the maximum shear stress under the surface.

The contact area depends on the geometry of the contacting bodies, load and material properties. In many cases, the contact area is enveloped by an ellipse such as in the case of two cylinders with different diameters, crossed at an angle $\neq 90°$ (when the

diameters are different, the contact becomes elliptical). It is important to note that when two cylinders have the same diameter, the contact is circular. The contact area between two parallel cylinders is enclosed by a narrow rectangle. Contact pressures and deflections also depend on the geometry of the contacting bodies.

In the present research work, the contact geometry between the Co28Cr6Mo samples and a tungsten carbide cylinder in the mechanical tests (where cold-hardening was performed) was defined by crossed cylinders positioned at approximately 90º as shown in Figure 2.1, taken from Popov (2010). Furthermore, in the tribological tests, the Co28Cr6Mo samples were also crossed at 90° with the ring-shaped zirconia counter bodies. It is important to note that, in this case, the contact area isn't circular but elliptical. This happens because the samples and counter bodies have different radii.
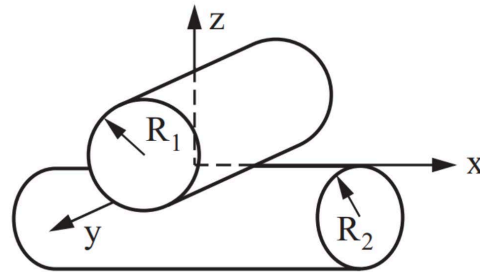
Figure 2.1. Contact between two crossed cylinders (Popov, 2010).

3. OBJECTIVES

As stated before, the objective of the present research work was to determine the optimal conditions that allow surface hardening of the Co28Cr6Mo alloy and consequently lead to increased wear resistance. However, preliminarily it was necessary to understand if this material presents favourable conditions for its hardening.

To understand whether a material is prone to hardening and to quantify this proneness, it is necessary to consider the definition of toughness. Toughness is the ability of a material to absorb energy and deform plastically without fracturing. A material with a high toughness allows favourable conditions for its hardening, i.e. mechanical treatments. This capacity varies from material to material and can be graphically represented by the area under the stress-strain curve of the material in question, as seen in Figure 3.1.
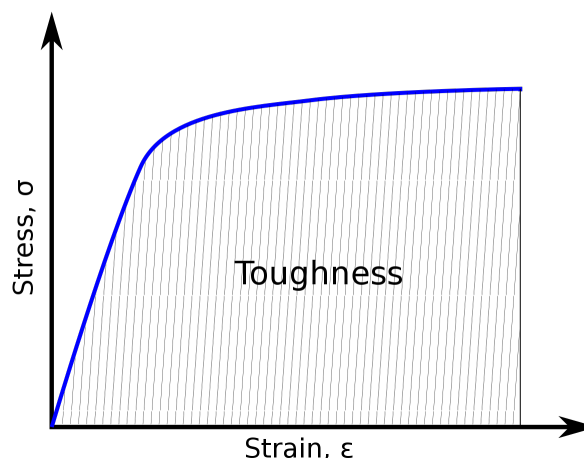
Figure 3.1. Toughness is the area under a stress-strain curve of a material.

Thus, it was necessary to analyse the stress-strain curve of the material of the present research work, Co28Cr6Mo, represented in Figure 3.2. This figure represents only the plastic domain of this material, since the area of the elastic zone is minimal, due to a very steep slope of the graph in this zone.
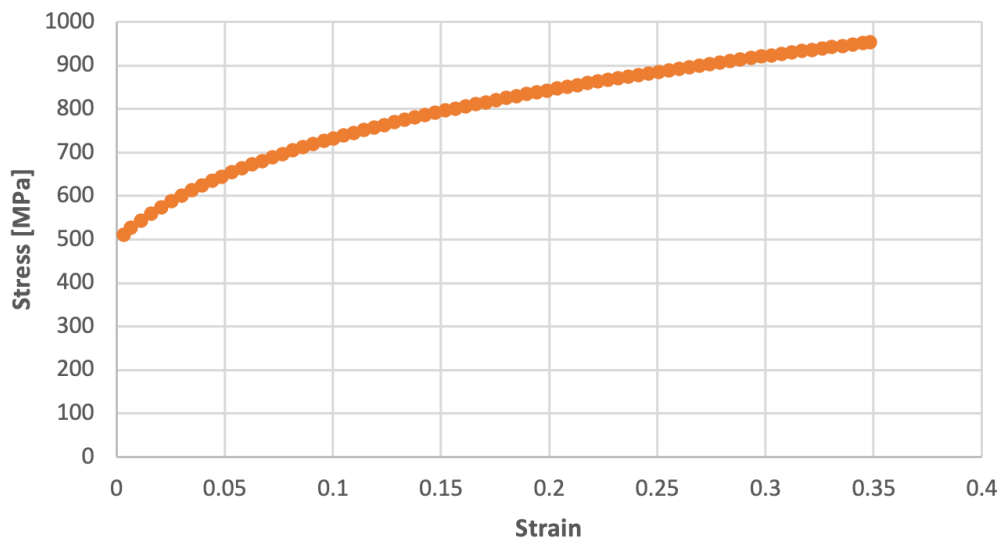
Figure 3.2. Plastic domain of the Co28Cr6Mo stress-strain curve.

As can be seen, there is a large difference between the yield strength (503 MPa) and the ultimate tensile strength (952 MPa). The area of the graph between these two values represents the extent associated with the strain hardening (Figure 3.3). The greater this difference, the greater its ability to harden. Thus, this Co28Cr6Mo alloy proves to be favourable for mechanical treatment as it has a very high toughness.
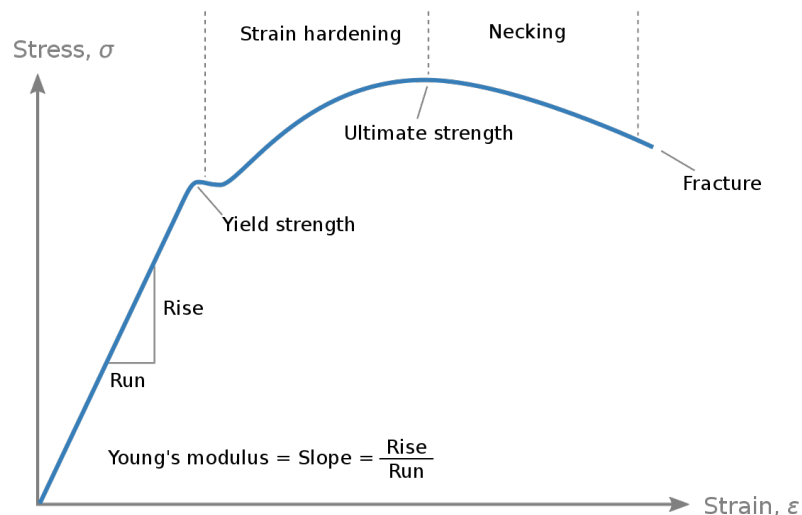
Figure 3.3. The extent between the yield strength and the ultimate tensile strength represents the strain hardening zone of the material.

As the material is work hardened it becomes increasingly saturated with new dislocations, and more dislocations are prevented from nucleating (a resistance to disloca-

tion-formation develops). This resistance to dislocation-formation manifests itself as a resistance to plastic deformation; hence, the observed strengthening. This leads to an increase in the yield strength of the material and a subsequent decrease in ductility. Upon application of stresses just beyond the yield strength of the non-cold-worked material, a cold-worked material will continue to deform. This justifies the usefulness of cold hardening in the wear resistance of the material.

The hardening of this Co28Cr6Mo alloy is particularly important for the purpose of this research work as it promotes increased wear resistance (it allows a lower wear rate) which is the ultimate objective since this alloy is used in biomedical applications and its longevity on human body is essential for the patient's life quality.

4. MATERIALS, EQUIPMENT AND PROCEDURES

4.1. Materials

4.1.1. Samples

The samples used in the present research work are made of Co28Cr6Mo cast alloy (also known as ASTM F75). The samples have a cylindrical geometry, with a diameter of 5 mm and a length of 10 mm. Its chemical composition and mechanical properties are shown, respectively, in Table 4.1 and Table 4.2. The values shown here were taken from the Standard Specification for Co28Cr6Mo Casting Alloy for Surgical Implants (UNS R30075).

Table 4.1. Chemical composition of Co28Cr6Mo alloy (ASTM F75).

	Chemical Composition (wt. %)	
Element	**Min**.	**Max**.
Chromium (Cr)	27	30
Molybdenum (Mo)	5	7
Nickel (Ni)		0.5
Iron (Fe)		0.75
Carbon (C)		0.35
Silicon (Si)		1
Manganese (Mn)		1
Tungsten (W)		0.2
Phosphorus (P)		0.02
Sulphur (S)		0.01
Nitrogen (N)		0.25
Aluminium (Al)		0.1
Titanium (Ti)		0.1
Boron (B)		0.01
Cobalt (Co)		Balance

Table 4.2. As-cast mechanical properties of Co28Cr6Mo alloy (ASTM F75).

Mechanical Properties	
Ultimate tensile strength (UTS), min.	655 MPa
Yield strength (YS, 0.2% offset), min.	450 MPa
Elongation, min.	8%
Reduction of area, min.	8%
Hardness	25-35 HRC 266-345 HV

4.1.2. Counter bodies

The counterbody used for the first experimental tests, namely, for the lathe mechanical tests, as explained in Section 4.3.2 (pg. 31), was a tungsten carbine (WC) cylinder, characterized by high hardness, in order to be close to the rigid material considered in the numerical model, also explained in Section 4.3.1 (pg. 28). This high hardness was essential to cause hardening of the Co28Cr6Mo samples.

On the other hand, for the sliding wear tests performed on the tribometer, a zirconia ring counter body was used against the Co28Cr6Mo sample (zirconia was chosen because it is commonly used as counter body on prostheses). Its external diameter was 20 mm.

4.2. Equipment

4.2.1. Lathe

In order to induce a superficial hardening of the Co28Cr6Mo specimens, a lathe was used to promote the rotation and the force between the crossed cylinders, as shown in Figure 4.1(a).

(a)
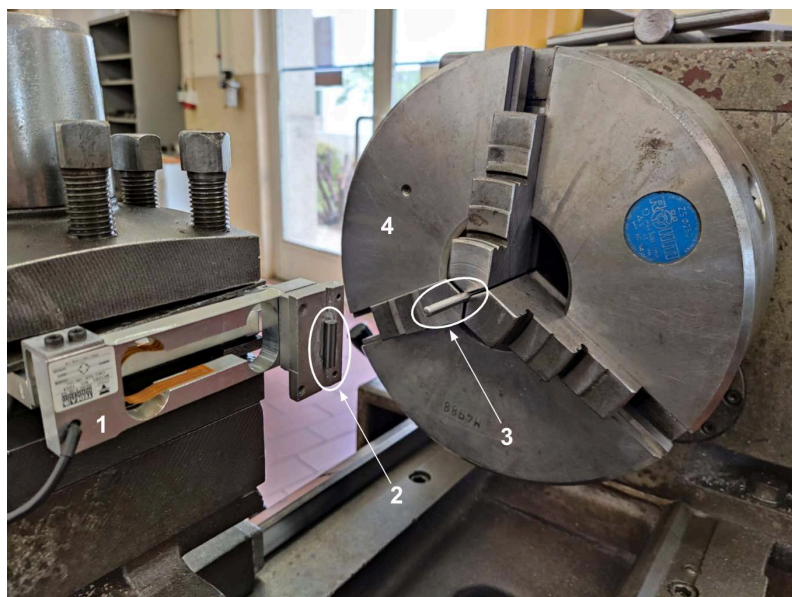
(b)

Figure 4.1. Equipment used during the mechanical tests.

Figure 4.1(b) shows a larger magnification of the equipment used. The respective legend follows:

1. Load cell;

2. Cylindrical tungsten carbide (WC) sample;

3. Co28Cr6Mo cylindrical sample;

4. Mechanical lathe to rotate the Co28Cr6Mo cylinder.

4.2.1.1. PicoScope

A PicoScope 3204A was used to view and analyse real-time signals. The PicoScope 6 software enables analysis using FFT, a spectrum analyser, voltage-based triggers, and the ability to save/load waveforms to disk. This equipment allowed to obtain voltage outputs that had a linear relation with the normal force and the frictional force, as described in Section 4.3.2 (pg. 31). Therefore, it ultimately allowed to determine the progression of these two variables through the experimental lathe test. Its outputs were later analysed: medium normal force and coefficient of friction were determined, averaging the instant values obtained during the mechanical tests.

4.2.2. Polisher

After cutting the samples in the hardened zone, they were polished in order to decrease the superficial rugosity of the cross section and obtain accurate Vickers micro hardness measurements in the durometer. After using a SiC Struers FEPA P # 1000 with 18 μm grain size, the sample was polished with a SiC Struers FEPA P # 2000, 10 μm. Additionally, a monocrystalline diamond suspension with 3 μm was applied.

4.2.3. Durometer

The hardness measurements were performed with a Struers Duramin durometer, shown in Figure 4.2. It has a maximum resolution of 0.01 μm and performs measurements on Vickers, Knoop, Brinell and Rockwell. In this case, these measurements were taken through Vickers micro hardness tests. This equipment is able to perform micro and macro-hardness measurements, with an applied load range of 10-2000 gf and automatic load system. The positioning of the samples is controlled by a micrometric measuring table with two degrees of freedom.
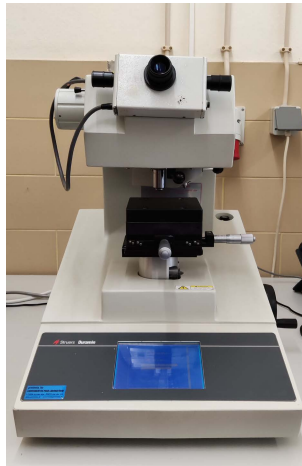
Figure 4.2. Struers Duramin durometer.

4.2.4. Scanning Electron Microscope

A scanning electron microscope (SEM) is a type of microscope that creates images of a determined specimen by scanning its surface with a focused beam of electrons that are generally produced in a tungsten filament. The electrons interact with atoms in the sample surface, producing various signals that contain information about the surface topography and composition of the sample. This equipment is also important to quantify in percentage the chemical composition of a certain pre-selected area of the material under analysis. The model used was a HITACHI SU3800 as shown in Figure 4.3.

Figure 4.3. HITACHI SU3800 scanning electron microscope.

4.2.5. Tribometer

A tribometer is used to carry out sliding wear tests in order to study lubrication, friction and wear. It allows the determination of different tribological quantities, namely the coefficient of friction, frictional force, and wear volume between two surfaces in contact. The tribometer used in the present research work was built in the Department of Mechanical Engineering of the University of Coimbra, based on a lathe. For the present study, the hertzian contact between two cylindrical surfaces was considered, the Co28Cr6Mo sample and a zirconia ring. The model used in this research was the Einhell BT-ML300 in which the zirconia ring surface rotated against, and perpendicularly to, the CoCrMo alloy sample.

Figure 4.4 and Figure 4.5 show the equipment used during the tribological tests. The respective legend follows:

- 1- Total rotation counting system;
- 2- Set of weights;
- 3- Zirconia ring;
- 4- Co28Cr6Mo sample;
- 5- Load cell (connected through wire to the set of weights).

Figure 4.4. Tribological tests' equipment used.
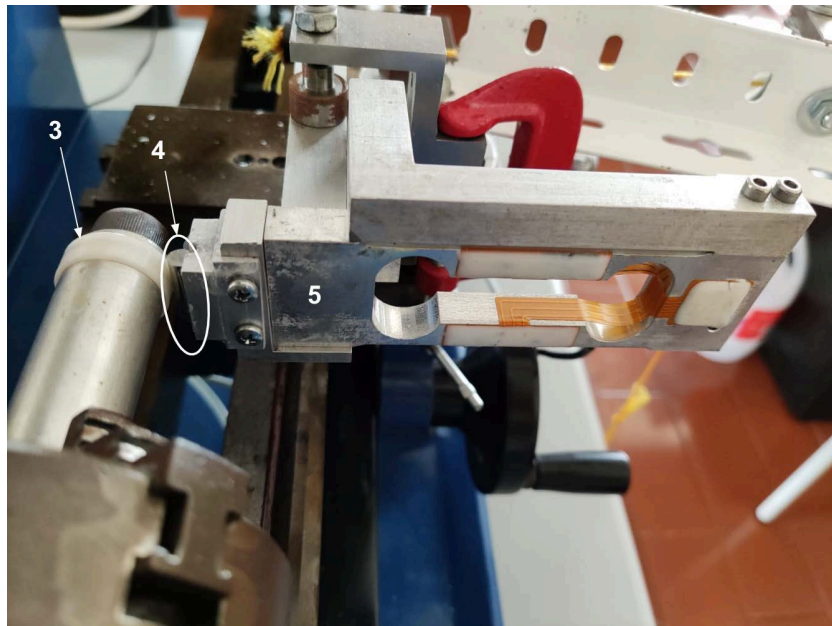
Figure 4.5. Tribological tests' equipment used: magnification of the contact area between the zirconia ring and the Co28Cr6Mo

The tribometer works by rotating a cylinder around its axis, on which, in this case, the zirconia ring is located. Being in contact with the Co28Cr6Mo specimen, it promotes its wear. This device has a system to count the number of revolutions performed.

4.2.6. Measuring microscope

Wear marks measurements were determined using a Mitutoyo Toolmaker's Microscope optical microscope (Figure 4.6), with 15x magnification and illumination with a circular lamp. It has a Microstage, a positioning system for the measuring plate, which holds two digital micrometers, one in each XY direction (two degrees of freedom), with an accuracy of 0.001 mm. Thus, using this equipment, it was possible to measure two diameters perpendicular to each other: the distances between the furthest ends and the closest ends, in the wear marks' ellipse. These measures allow the subsequent determination of the wear volume.

Figure 4.6. Mitutoyo Toolmaker's Microscope

4.3. Methods and procedures

4.3.1. Numerical model

The numerical model created was intended to study the surface hardening of the Co28Cr6Mo alloy (its generic aspect can be seen in Figure 4.7). The impact of model variables variation on the stresses could be analysed. It was designed to obtain a better initial approximation of favourable conditions for the mechanical tests.

The software adopted was DD3IMP and it is used to perform numerical simulation of plastic metal forming processes. Since it is dedicated to sheet metal stamping, it is necessary that the mechanical model contemplates the elastoplastic behaviour of the material, namely the deformations and rotations to which the metal is subjected. The elastic behaviour is considered isotropic while the plastic behaviour can be anisotropic, using several plasticity criteria and strain hardening laws. The DD3IMP software considers that the effects of inertial forces are neglected. In terms of the type of elements used, DD3IMP only allows to discretize with solid finite elements, being required to use at least two layers of elements in thickness to allow a correct description of the stress gradients in this direction.

The main results of the model, represented graphically, are:

- The evolution of the plastic deformation value with the passage number;
- The effect of the coefficient of friction on the plastic deformation value and on the distribution of shear stress xy;
- The effect of normal force on the plastic deformation value and on the distribution of

shear stress xy.

In addition to all graphical representations, the distribution of plastic deformation along the radial direction at the end of each passage was analysed, comparing the passages with each other. This procedure was taken into account in order to ascertain whether the depth of the plastic deformation increases with the number of passages.

The numerical model developed had the following characteristics:

- Positioning of two crossed cylinders: one rigid and the other deformable (this last cylinder with the approximate mechanical properties of the Co28Cr6Mo alloy).

- Deformable cylinder with 5 mm diameter and 10 mm length and recessed at its ends (with rotation imposed on them).

- Due to the condition of symmetry, only half model (half cylinder length) is simulated.

- The mesh of the zone under study of the Co28Cr6Mo cylinder is much more refined compared to the rest of the model. Only ¼ of the cylinder perimeter is analysed (since the behaviour is always identical along the perimeter and thus the time of the simulations is significantly reduced). Plus, the superficial zone of this mesh is much more refined than the subsurface and more interior zones. This means that there is a much closer approximation of what is happening at the surface than what can be concluded from what is happening inside the cylinder.

- Variables: normal force (indirectly, because the real variable is the displacement of the cylinder that comes into contact), coefficient of friction, number of passages (with a maximum of 5).
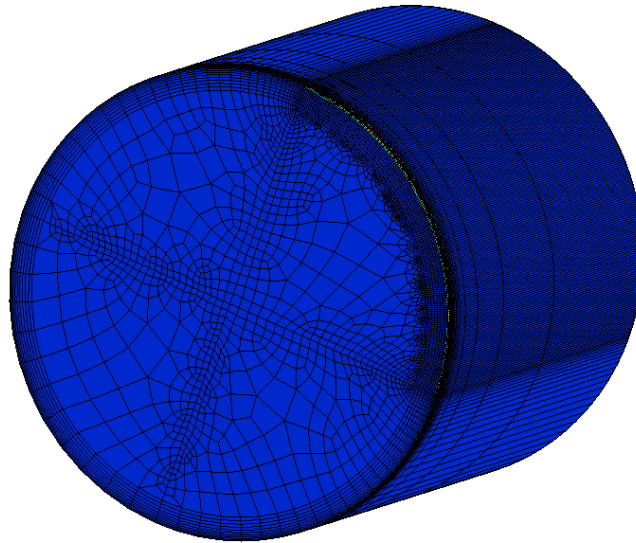
Figure 4.7. Generic aspect of the numerical model, with the most refined mesh in the analysed area.

When running the numerical model, it presents different phases of movements. Each phase is associated with an iPH value. These phases are cyclical, that is, they occur in a loop until the total value of passages defined at the beginning of the simulation is reached (this being one of the variables). The sequence of phases during a simulation is:

- iPH = 1 corresponds to a 45º rotation in the positive direction (counterclockwise); initially, the model's cylinder is at -45º.

- iPH = 2: The rigid surface touches the deformable cylinder at the maximum x coordinate (normal direction) at an angle of 90º with the horizontal. Before starting the sweep, a displacement is made in this direction until half the value of the desired force is obtained, because only half the cylinder length is considered. This phase therefore corresponds to a tightening between the two cylinders.

- iPH = 3: When this half of the desired force is reached, the position is maintained and the cylinder is rotated 90º clockwise (1 pass thus corresponds to ¼ of the cylinder).

- iPH = 4: Corresponds to a rotation backwards (counterclockwise), after total removal of the rigid surface (which simulates an empty passage). This empty passage is made to ensure that the slip always occurs in the same direction (clockwise). It is important to note that it does not rotate -90º (which would be the initial position) but, for example, in the case of the end of the first pass, -85º, that is, with a difference of 5º. The first passage has an amplitude of 90º, the second of 80º, the third of 70º and the

fourth of 60º (reduction of 5º in each of the ends, totaling 10º). This reduction in scanning amplitude was taken into account to start the next passage in a stable area; that is, for the new passage to start in an area where the plastic deformation caused by the previous passage is uniform (at the beginning of each sweep there is a transition zone, not yet uniform). Thus, the scanning line is shortened as more passes are made (there is a gradual decrease in amplitudes, as seen in Figure 4.8).
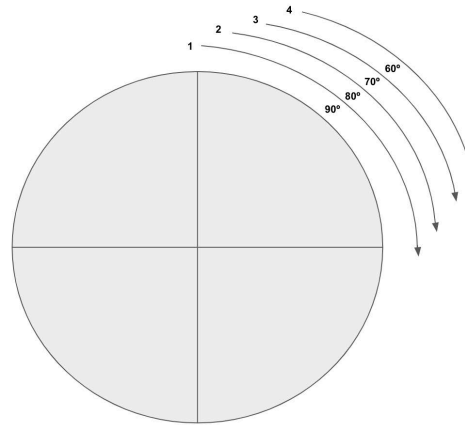
Figure 4.8. Simplified representation of the successive reduction in range of motion with the passage number.

The reduction of 5º on each side, in each it iteration (passage) of the process, is more than enough, clearly delimiting the transition zone of the uniform plastic deformation zone. It is an "excessive" value, which does not cause any limitation in the number of passages since the tests will have a maximum of 5 passages.

4.3.2. Lathe mechanical tests to induce strain hardening

In the mechanical lathe tests, a Co28Cr6Mo cylinder (d= 5.02 mm) was positioned crossed against a cylinder of a much higher Young's modulus material (a tungsten carbide, WC) in order to simulate a rigid body (considering a rigid body was assumed in the numerical model). This WC cylinder was attached to a load cell, as shown previously in Figure 4.1(b) in Section 4.2.1 (pg. 22), through which voltage values would be captured, transmitted to PicoScope 6 software as outputs and later converted into normal force and frictional force. There was axial and rotational movement of the Co28Cr6Mo cylinder (axial speed was 68 μm/turn and n=170 rev/min). The axial movement of the Co28Cr6Mo cylinder relative to the WC crossed cylinder had to be necessarily slow enough to have contact between the two along the entire lateral cylindrical area when sweeping; otherwise,

there would be areas of the sample to be hardened that would not undergo this treatment. Hence, a reduced axial velocity was selected. Ten passages were taken into account in every test: each passage corresponds to the axial scan of a pre-defined distance (between two black lines previously drawn on the specimen, Figure 4.9).

Figure 4.9. Top view of the contact between the Co28Cr6Mo and the WC cylinders. The Co28Cr6Mo cylinder is connected to the lathe, which gives it rotational and forward movement. Its sweeping area is delimited by the black marks.

The PicoScope 6 software used gathered the outputs (a two-list output: list A corresponding to the frictional force and B corresponding to the normal force). This output results came in voltage SI units (Volt); therefore a conversion was needed between the voltage values and their respective force values, in Newton:

$$Frictional\ Force = \frac{Voltage\ Output\ A}{0.8003} \qquad (4.1)$$

$$Normal\ Force = \frac{Voltage\ Output\ B}{0.4162} \qquad (4.2)$$

The constants, 0.8003 and 0.4162, were determined before starting the tests. Weights were added to the load cell in both the normal and tangential directions, a calibration curve was drawn and the slope was determined.

The coefficient of friction was after calculated with the following expression:

$$Coefficient\ of\ Friction = \frac{Frictional\ Force}{Normal\ Force} \tag{4.3}$$

3 mechanical tests were carried out with different parameters of normal force and coefficient of friction, calculated through the Excel processing of the outputs provided by PicoScope 3204A hardware and saved through PicoScope 6 software. After this processing in Excel, the values of average normal force, frictional force and, consequently, coefficient of friction were obtained and it was possible to characterize the 3 tests as follows, in Table 4.3.

Table 4.3. Normal force and coefficient of friction values for each mechanical test.

Mechanical Test	2	3	4
Normal force [N]	19.79	10.57	5.93
Coefficient of friction	0.221	0.147	0.145

It is important to note that Mechanical Test 1 was rejected as it was only performed for 5 passages. Thus, it was intended to eliminate this variable (number of passages), avoiding to increase the number of factors that could influence the results and respective interventions; this simplification was considered in all the other mechanical tests (2, 3 and 4) for 10 passages.

The values obtained for the normal force were not random. Initially, it was intended to analyse the behaviour of this alloy, Co28Cr6Mo, for an approximate normal force of 20 N. After verifying that this value was unreasonable and was associated with unfavourable hardening conditions, explained below in Section 5.2.2 (pg. 57), the normal force in the following mechanical tests has been reduced. Thus, this decrease from test to test is justified.

4.3.3. Radial hardness analysis

After cutting the sample of Co28Cr6Mo in the mechanically treated section and later polishing the area to be analysed (the cross section area), it was placed in the Struers Duramin durometer to quantify the evolution of the hardness through the sample's radius (schematically represented in Figure 4.10), that is, see the influence of the mechanical hardening on the hardness of the cylindrical specimen. Several indentations (with a

force value of approximately 1 N) were made over a diameter of the cross section of the sample, in diamond shape (Figure 4.11). Measuring the diagonal distances and, consequently, the indentations area, Vickers hardness values were obtained. This procedure was taken not only with the samples from the mechanical tests (2, 3 and 4) but also with an untreated (that is, untested) sample, that was not subjected to mechanical superficial hardening. With these several indentations and their respective hardness values, radial hardness evolution graphics were created in Excel, which made possible a comparison between the different treated samples and the original unhardened sample.

Figure 4.10. Schematic representation of the hardness analysis in the radial direction of the Co28Cr6Mo samples.
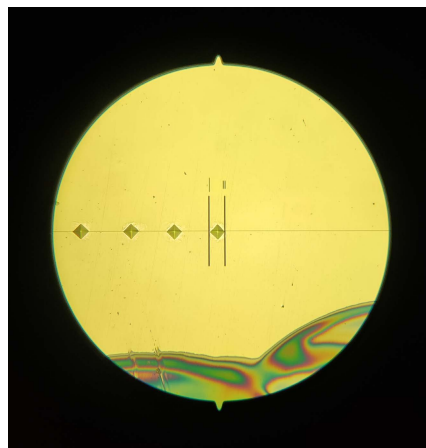
Figure 4.11. Vickers hardness measurements being performed on the Struers Duramin equipment.

It should be noted that, before this radial analysis, hardness values were obtained from areas close to the centre in order to obtain an average hardness value of these CoCrMo alloy samples. It was found that this samples had an average hardness of 453 kgf/mm^2 (HV$_{0.1}$), with a standard deviation of 14.7 kgf/mm^2. This value of hardness is higher than the value stated in the Standard Specification for Co28Cr6Mo Casting Alloy for

Surgical Implants (UNS R30075), from Table 4.2 in Section 4.1.1 (pg. 21), which might indicate that the samples came already hardened to a certain degree, from their supplier.

4.3.4. Etching and SEM analysis of the cross section

Etching is a preferential corrosive attack on the areas of greatest energy on the metal surface in contact with the etchant, that is, the grain boundaries; it is therefore essential to highlight the grain boundaries of the treated samples. For this alloy, it proved to be a complicated task, since it has a high corrosion resistance. Although some bibliography (Chauhan, 2017) indicates that best results are obtained by electrolytic etching for 15-30 seconds in 30% HCl solution with few drops of H_2O_2 at 4V and graphite electrode, it was found that this etching time was not enough. Thus, by trial and error approach, the contact time of the solution with the alloy was extended to 1 minute.

After etching the Co28Cr6Mo specimens, they were placed in the Scanning Electron Microscope (SEM) in order to visualize the grain size and orientation on their cross section (as represented in orange colour in Figure 4.12), especially in the most peripheral areas (those, which, hopefully, would be the most affected by the cold hardening during the mechanical tests). As said earlier, a SEM equipment produces an image from the interactions of the electron beam with atoms at various depths within the sample. The electron beam is scanned in a raster scan pattern, and the position of the beam is combined with the intensity of the detected signal to produce the image (Figure 4.13 is an example of a SEM produced image). The samples were visualized in high vacuum. Using a computer and accessing Hitachi software, it was possible to save the images collected by SEM.

This procedure allowed to reinforce and validate the results obtained in the radial hardness analysis, revealed in Section 5 (pg. 43).
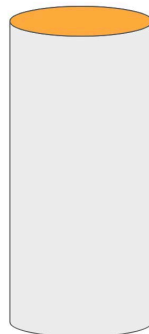

Figure 4.12. Co28Cr6Mo samples' cross section schematic representation, in orange colour; both etching and SEM analysis were performed in this area.
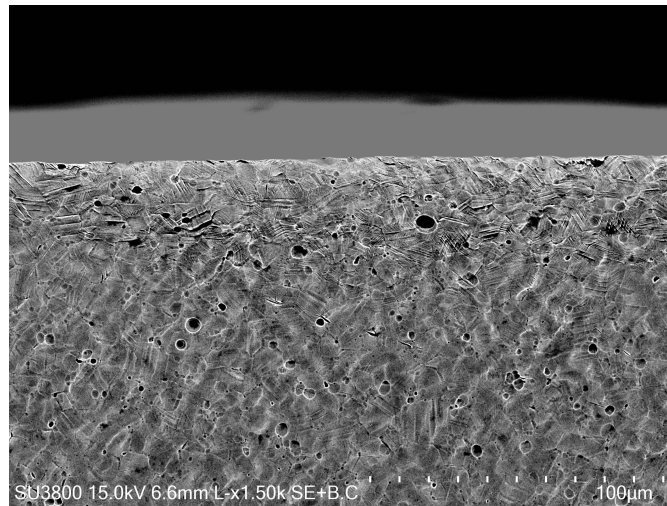
Figure 4.13. Example of a collected SEM picture of Co28Cr6Mo alloy after being subject to strain hardening with an applied normal force of 19.79N (Mechanical Test 2).

4.3.5. Tribological Tests

The tribological tests quantified the final wear and the coefficient of friction throughout each test. These tests were carried out for four different Co28Cr6Mo cylindrical samples: an untreated sample (mechanically untested) and the three cold-worked samples on the lathe from mechanical tests 2, 3 and 4.

These tribological tests consisted of rotating a zirconia ring against the lateral section of the Co28Cr6Mo specimens, keeping the cylinders with crossed axis. Note that this side section corresponds to the area of material that was in direct contact with the WC cylinder when submitted to cold hardening. This rotation promotes wear and consequent removal of material from the Co28Cr6Mo cylinder; the purpose of this procedure is to later analyse and quantify this material removal and verify its variation with the increase of the applied normal force, that is, with the increase of the perpendicular contact force between the specimen and the zirconia ring during the tribological tests.

It was necessary to monitor what happens during the time of each test (that had a total duration of 6818 seconds). Thus, with a load cell coupled to the tribometer structure, as seen above in Figure 4.4 in Section 4.2.5 (pg. 26), and connected to a computer it was possible to read and record the instantaneous frictional force.

On that computer, an interface was programmed in Labview 8, which allowed to control the operation of the tribometer and to consider the variables whose values can be changed by the users (for example, the applied normal force or the test time; although, in

this case, the test time was always the same). However, it should be noted that, in this case, the only variable changed before each tribological test was the normal force. This normal load is applied manually, through a set of weights (as can be seen in Figure 4.14), indirectly connected to the load cell by a wire and a pulley (1 N, 2 N, 4 N, 6 N, 8 N, 10 N and 12 N were applied, in different tests, to the untreated and the treated samples as well). The desired total number of rotations was 20000; therefore, a rotation counting system was also implemented to verify, for each test, if 6818 seconds corresponded to approximately this number of rotations (n=175 RPM).
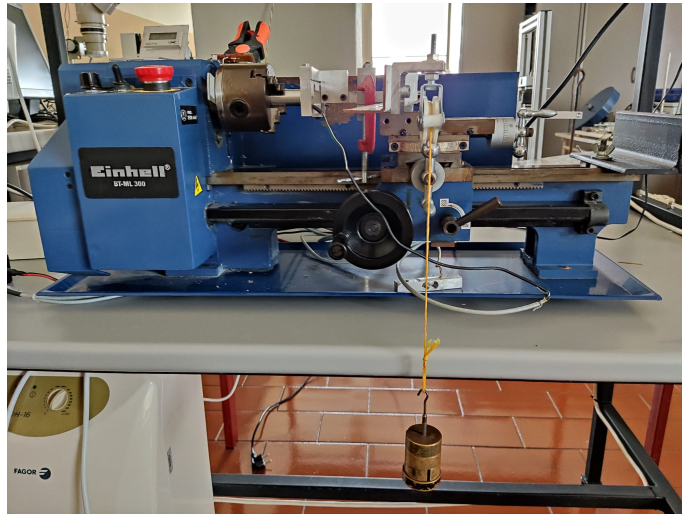
Figure 4.14. Tribometer used during wear tests: the set of weights applied, according to the desired normal force, is connected to the load cell by a wire, which in turn has the Co28Cr6Mo sample attached to it.

4.3.5.1. Samples' removed volume analysis

After the tests on the tribometer, the Mitutoyo toolmaker's microscope was used to visualize the contact zone (Figure 4.15). As explained before, this contact zone was an ellipse and, with the help of two digital micrometre rules, the lengths of the respective major and minor axis were determined. These distances were needed to evaluate the volume of Co28Cr6Mo removed during each test.
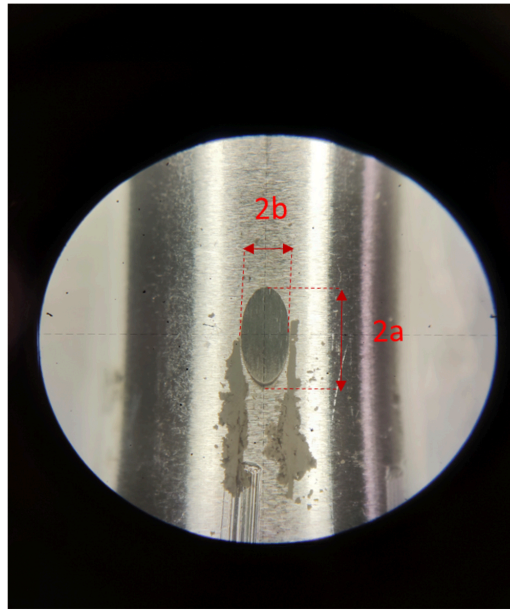
Figure 4.15. Contact zone observed through Mitutoyo toolmaker's microscope, after a tribological test.

Considering R_1 the external radius of the zirconia ring, R_2 the radius of the Co28Cr6Mo ASTM F75 sample, a and b respectively the semi-major and semi-minor axis of the ellipse (Figure 4.15 and Figure 4.16), h' and h'' the maximum depth of the contact zone, analysed in two perpendicular plans:

$$h' = R_1 - \sqrt{R_1^2 - a^2} \tag{4.4}$$

$$h'' = R_2 - \sqrt{R_2^2 - b^2} \tag{4.5}$$

$$h = \frac{h' + h''}{2} \tag{4.6}$$
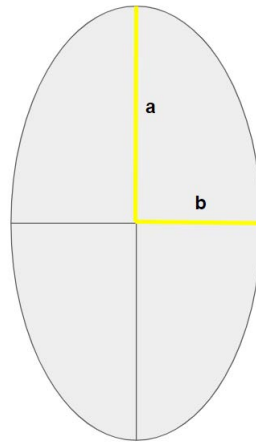
Figure 4.16. Schematic representation of distances a and b, on the elliptical contact zone.

V, as stated by A. Ramalho (2004), is the volume of material removed after each test, and x is the total sliding distance swept by the zirconia ring:

$$V = \pi \times h^2 \times \sqrt{R_1 \times R_2} \qquad (4.7)$$

$$x = Number\ of\ Rotations \times \pi \times 2R_1 \qquad (4.8)$$

Considering N as the normal force applied and k as the wear coefficient, V is also represented by:

$$V = k \times N \times x \qquad (4.9)$$

It was assumed that the equation above is linear. Therefore, V can be represented in order to x' where k is the slope:

$$x' = N \times x \qquad (4.10)$$

$$V = k \times x' \qquad (4.11)$$

Using Excel it was possible to create, both for the untreated sample and for the mechanical tests 2, 3 and 4, a graph of the volume removed from the samples as a function of x', V(x') as seen below in Section 5.2.2 (pg. 57). The main focus for this procedure was to associate the wear coefficient to be calculated, k, with the slope of a linear relationship (A. Ramalho, 2010). This variable became useful to quantify wear.

4.3.5.2. SEM and optical microscope analysis of oxides

As will be seen below in Section 5 (pg. 43), the results obtained for the tribological tests suggest that, from a given normal force, the volume of material removed from

the wear zone of certain mechanical tests' samples increases significantly. It was decided to look for a justification for this sudden increase, since the volume of material removed has a certain linearity but only up to a certain value of normal force applied, from which it reveals a much more accentuated slope. It was also decided to try to explain why not all Co28Cr6Mo samples show this exponential volume increase in removed material.

The purpose of this procedure was to verify whether the existence of oxides at the highest normal force values could have influenced the results of the volume of material removed in the tribological tests, namely if it would have functioned as a protective film for this Co28Cr6Mo alloy in the samples of the mechanical tests with a less pronounced increase of the volume removed between different applied normal forces.

Thus, the wear marks of the tribological tests were analysed in SEM, since this equipment not only allows a good visualization of possible oxides, through BSE mode, but also provides the chemical composition, through EDS analysis, of a given area under examination; if there are oxides in the wear marks, oxygen will be present in high percentage in these areas, validating this theory. It should be noted that these marks were also visualised through an optical microscope.

The Figure 4.17 represents schematically the zones of the samples under analysis, in orange colour. Again, and as mentioned above, the contact zones between the Co28Cr6Mo specimen and the zirconia ring are elliptical, as they have different radii. Furthermore, this schematic representation reveals different dimensions of these elliptical contact zones, since the variation of the normal force applied between tribological tests causes a variation in the volume of material removed (which is directly linked to different wear mark dimensions).
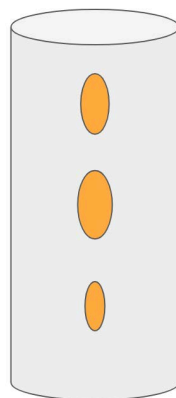
Figure 4.17. Schematic representation of the wear marks, in orange colour, under analysis.

4.3.5.3. **Microscopic analysis of oxide fixation in zirconia rings**

As the tribological tests are based on continuous contact between the rotating zirconia ring and the Co28Cr6Mo sample, the analysis of the oxide formation on the wear marks of the specimen can be supplemented with the analysis of the trace created on the zirconia rings. These traces can be expected to be a mixture of abrasion and some oxides released by the specimens during the tests. The aim of this procedure was to verify the amount of oxides in the trace created along the perimeter of the zirconia ring, comparing the results with what can be seen in the respective wear marks of the Co28Cr6Mo specimen. Hopefully, wear marks on these Co28Cr6Mo alloy specimens with high amounts of oxides can be expected to be associated with marks on the zirconia ring with a high concentration of oxides as well.

5. RESULTS AND DISCUSSION

5.1. Strain hardening

5.1.1. Numerical modelling

As previously mentioned, the numerical model was designed to obtain a better initial approximation of favourable conditions for the mechanical tests of surface hardening. Preliminarily, the numerical model allowed to reach some conclusions concerning, for example, the influence of the number of passages on the depth of the deformed surface layer of the Co28Cr6Mo cylinder or the influence of the coefficient of friction, strain or flow stress (instantaneous value of stress required to continue plastically deforming a material) also on the extent of deformed material.

Figure 5.1 represents the comparative graph between two simulations in which the same normal force was applied, differing only in the coefficient of friction. Through its analysis it is possible to verify that although Simulation 2 has higher strain values in a certain extension, a higher coefficient of friction does not lead to more extensive deformed zones; its variation does not cause any significant change in the depth of the deformed surface zone. Analogous conclusions can be drawn through a flow stress comparative graph, as can be seen in Figure 5.2.
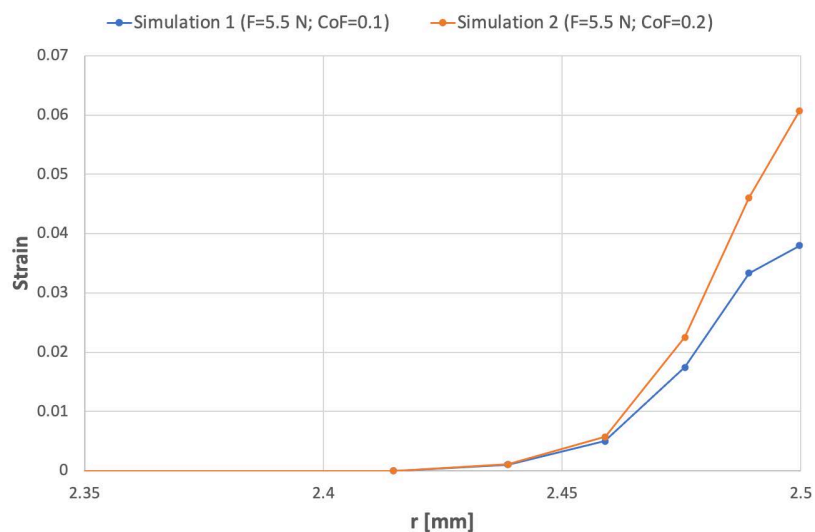

Figure 5.1. Influence of the coefficient of friction (CoF) on strain and on the depth of the deformed surface layer of a Co28Cr6Mo simulated cylinder.

Figure 5.2. Influence of the coefficient of friction (CoF) on flow stress and on the depth of the deformed surface layer of a Co28Cr6Mo simulated cylinder.

Both Figure 5.1 and Figure 5.2 show that not only the variation of the coefficient of friction does not change the depth of the plastically deformed zone but also this layer is relatively superficial. In fact, this zone extends only about 80 μm towards the centre of the cylindrical Co28Cr6Mo sample. This extension represents about 3.2% of the distance between the periphery and the centre of the sample. Again, a surface hardening only is intended, that is, an improvement of the mechanical properties only at the surface of the material. Thus, these numerical model results are consistent with the desired goal.

In addition to the previous analyses, the numerical model allowed to understand the influence of increasing the normal load from simulation to simulation on the depth of the plastically deformed Co28Cr6Mo cylinder surface layer. As can be verified in Figure 5.3, when maintaining the coefficient of friction constant, varying the normal load it is observed that, although the surface deformation reveals higher values for the higher values of force, the depth of the affected zone does not change. Thus, it was verified that the increase of the normal force, later on in the mechanical tests of strain hardening, would have no effect on the size of the plastically deformed layer. Analogous conclusions can be drawn through a flow stress comparative graph, as can be seen in Figure 5.4.
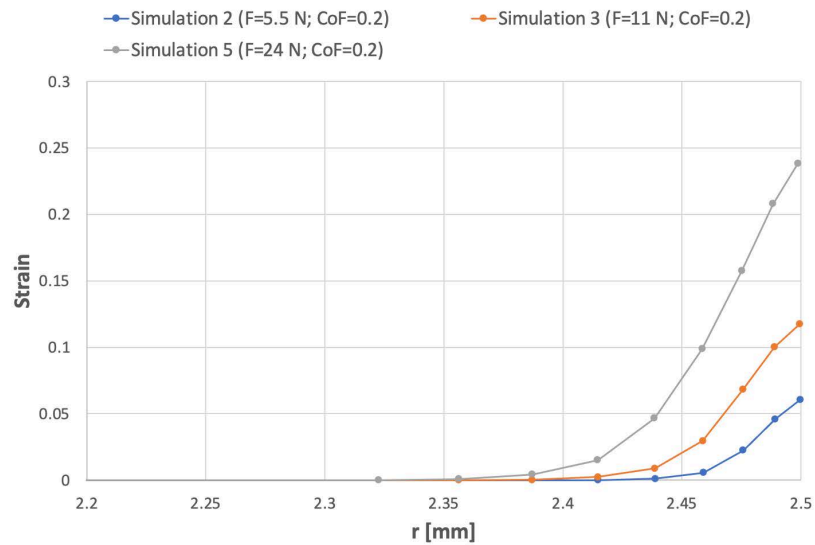
Figure 5.3. Influence of the normal load on strain and on the depth of the deformed surface layer of a Co28Cr6Mo simulated cylinder.
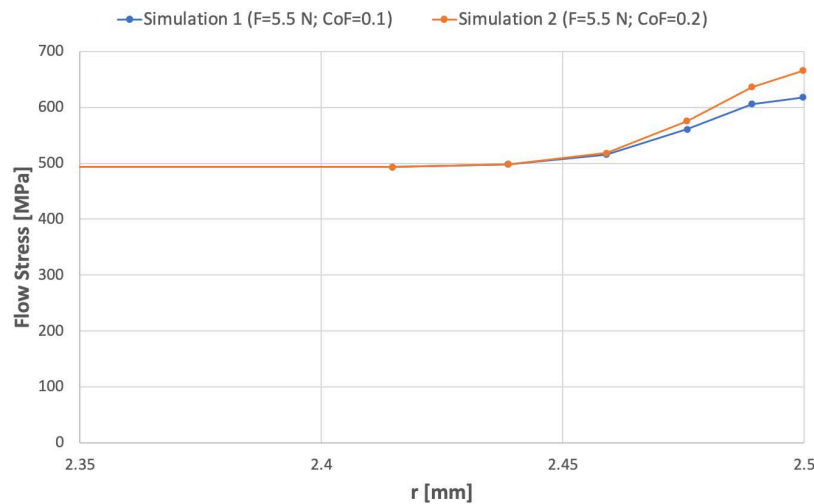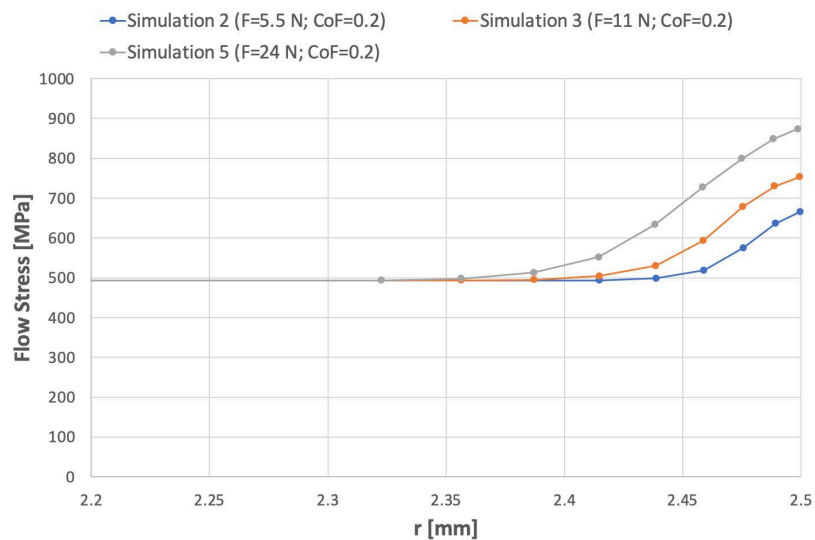

Figure 5.4. Influence of the normal load on flow stress and on the depth of the deformed surface layer of a Co28Cr6Mo simulated cylinder.

Although the numerical model allows drawing conclusions as mentioned above, its validity depends on the fact that the hardening occurs precisely at the surface during the experimental work. This is due to the fact that the numerical model mesh is refined only in the most peripheral areas of the cylinder created to simulate a Co28Cr6Mo specimen (the mesh of the innermost areas of the model presents a much lower accuracy of what happens, at the mechanical level). Therefore, and due to the importance of the mechanical treatment occurring superficially, it is necessary to verify that this hardening actually occurred in the most superficial layer possible of the samples. In Section 5.1.3.2 (pg.

50) this problem is analysed, using a simulation software to understand if, with the conditions that were possible to obtain in the mechanical tests, it was possible to obtain surface hardening only and, therefore, be in line with the numerical model programmed conditions.

5.1.2. Technologic Process

As mentioned previously in Section 4.3.2 (pg. 31), average normal force and coefficient of friction values were obtained for each of the three mechanical tests performed. It was found that, with the increase in the normal force applied, there was a consequent increase in the coefficient of friction (due to the greater tangential forces involved), as can be seen in Figure 5.5.
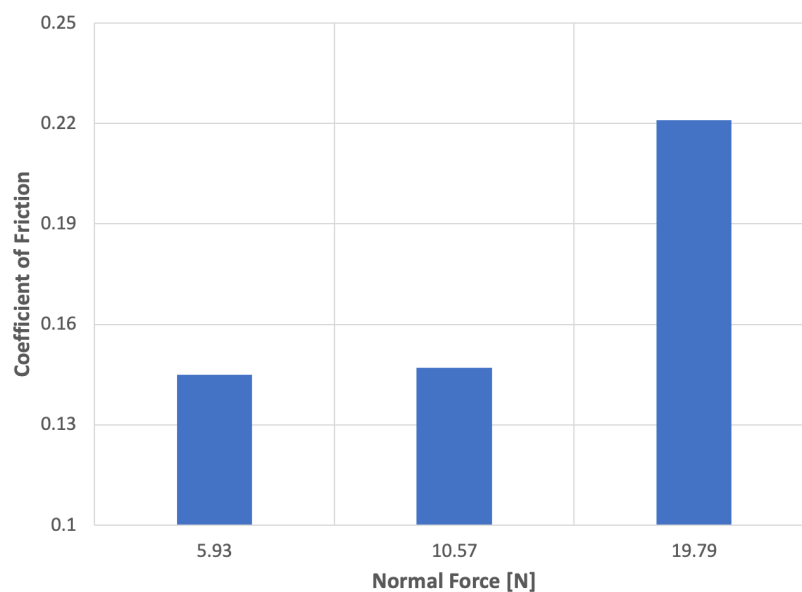
Figure 5.5. The increase of the normal force applied during the mechanical tests, between the tungsten carbide (WC) cylinder and the Co28Cr6Mo cylinder, lead to a visible increase of the coefficient of friction associated.

The determination of the average values of both the normal force and the coefficient of friction were obtained using the graphs of instantaneous values of each variable, for each passage made (it should be remembered that, during the mechanical hardening tests, a total of 10 scans between the WC and the Co28Cr6Mo specimens were performed).

Figure 5.6 represents the instantaneous evolution of the coefficient of friction associated to the sixth passage of the mechanical test in which a 5.93 N load was applied. There is a range of initial values that are discrepant from the others (i.e. relatively higher), throughout the determination of the instantaneous coefficient of friction. This is due to the initial running-in effect; that period was not considered in the calculation of the average value of this variable (only values after the first 10 second period, in this case, were con-

sidered). The same reasoning related to this running-in effect was taken for the determination of the average values of the normal force applied. Finally, for each mechanical test the final values of the coefficient of friction and normal force were obtained by averaging the mean values of each passage.
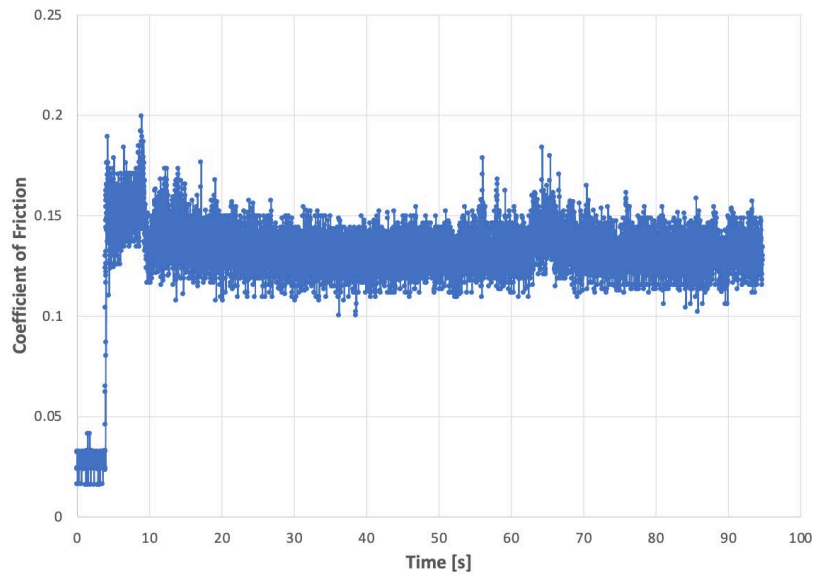
Figure 5.6. Instantaneous variation of the coefficient of friction, relative to the sixth passage of the mechanical hardening test in which 5.93N of normal force was applied.

The final results for the mechanical tests' mean values are in Table 4.3, above in Section 4.3.2 (pg. 31).

5.1.3. Strain hardening assessment

After performing the procedure described in Section 4.3.3 (pg. 33), it was possible to create a comparative graph of the samples' hardness evolution (three treated and one untreated samples) from the centre of the cross section of each specimen (circular section, since the samples are cylindrical) to the periphery, that is, to the most superficial area, where an increase in hardening was intended. The results of this hardness evolution allowed to quantify the influence of the conditions of each mechanical test on the mechanical properties of this Co28Cr6Mo alloy.

This graphical representation is depicted in Figure 5.7. Here, it is possible to see the different evolutions between the three mechanical tests under consideration and also in relation to the untreated sample. The origin of the horizontal axis corresponds to the centre of the cross section of the samples, and r= 2500 µm corresponds to the total radius. The resolution of the hardness profile was approximately 50 µm between indentations.
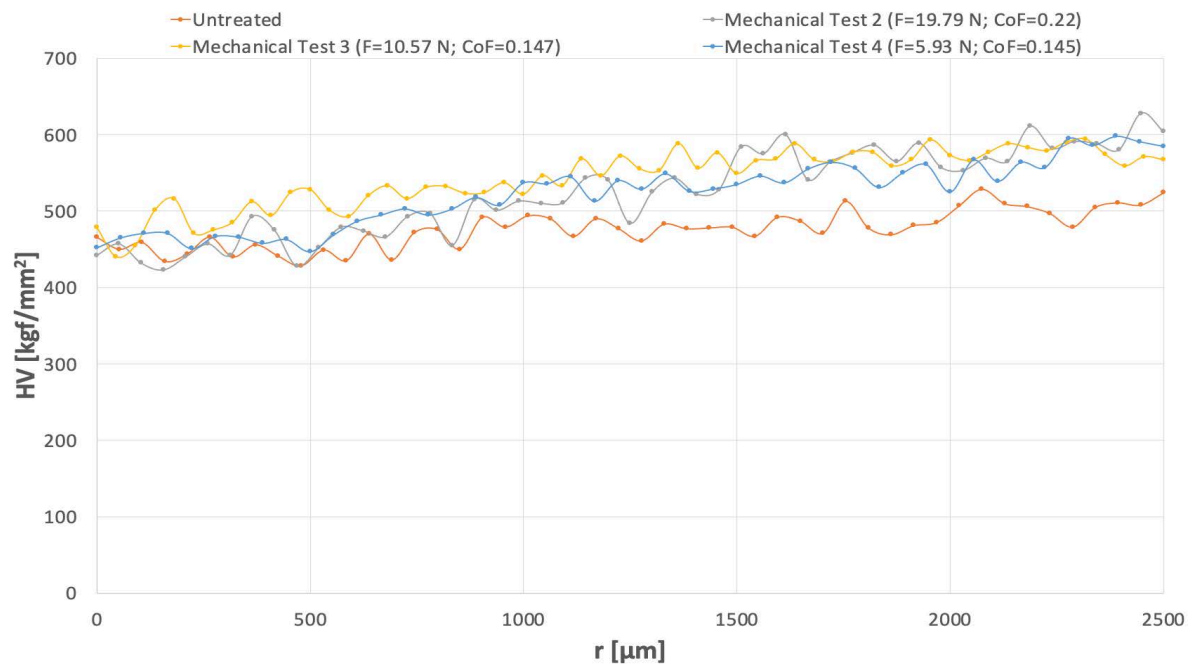
Figure 5.7. Evolution of microhardness with the radial distance for four different samples, three samples were subjected to different applied loads (5.93, 10.57 and 19.79N) and one remained as originally (untreated).

First, it can be seen that there is a slight increasing trend in the hardness of the untreated sample, from the centre to the periphery. This indicates that the samples already came from the supplier with a certain surface hardening. This hypothesis is also supported by what was previously mentioned regarding the average hardness at the centre of the sample: it was found to be higher than the tabulated hardness for Co28Cr6Mo ASTM F75. The untreated sample had a determined average hardness of 453 kgf/mm^2. The tabulated value, on the other hand is 266-345 kgf/mm^2. This means there was a 31.3-70.3% difference.

Regarding the results of the mechanical hardening tests, it is preliminarily verified that all of them present a more accentuated radial hardness evolution, comparing with the evolution of the untreated sample.

The test in which a normal force of 10.57 N was applied (Mechanical Test 3, yellow curve), clearly shows the highest average hardness values over the first 1500 μm, with a less pronounced increase from there to 2500 μm (which, again, represents the periphery of the cross-section of the sample).

Analysing the 500 μm closest to the periphery, there is a more accentuated hardness increase for the test in which a normal force of 19.79 N was applied (Mechanical Test 2, grey curve) compared to the tests where loads of 5.93 and 10.57 N were applied.

However, the average hardness value for this test, in that area, seems identical when compared to the test of 10.57 N normal force applied. On the contrary, the test of 5.93 N applied load (blue curve), presents not only a less accentuated increase in hardness from 2000 μm onwards, but also a visibly lower average hardness value, comparing to the other mechanical tests.

5.1.3.1. Strain hardened zones depth

The radial analysis of the hardness of treated samples allowed to verify its increase from the centre of the cross section to its periphery. However, the variation of the hardness with the distance to the surface doesn't agree with the results of the numerical model. In fact, numerical study forecasted an increase of the hardness up to 80 μm below the surface. This difference could be explained by the reduced resolution of the hardness profile, 50 μm between indentations as mentioned above. Therefore, to validate this increase in radial hardness, it was decided to analyse the cross section of each treated sample through SEM (Scanning Electron Microscope) which allowed a good visualization of the deformation of the grains in areas that have undergone cold hardening, through previous mechanical tests. This type of visualization allows not only to verify the areas with greater deformation, but also to verify the distance from the periphery that they occur. Figure 5.8 reveals the existence of clearly visible deformations of the grains, for the test in which a normal force of 19.79 N was applied (Mechanical Test 2). As can be seen, the zones of greatest grain deformation are not exactly at the surface of these samples, i.e. in the most peripheral zone possible. This means that these deformations are found at a certain depth; in an ideal situation they would be mainly on the surface since the aim is to obtain surface hardening only. This may influence the wear and removal volume results obtained in the tribological tests, revealed below.

(a)

(b)
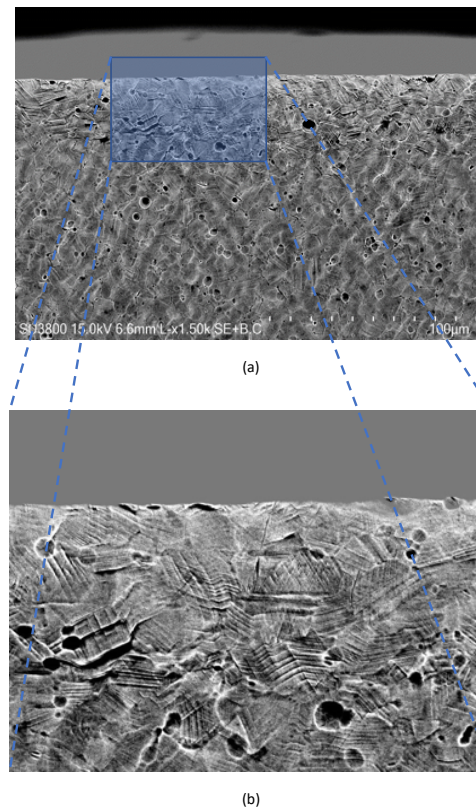
Figure 5.8. Visualisation through SEM of grain deformations, for the cross-section of the Mechanical Test 2 specimen, in this case: a) full micrograph and b) detail of deformed zone.

The images captured in the SEM related to the tests in which loads of 10.57 N and 5.93 N were applied (Mechanical Tests 3 and 4, respectively) also allowed to obtain results that showed a certain depth of the deformed zone.

5.1.3.2. HertzWin software and verification of depth of maximum shear stresses

As it was verified, the plastic deformations related to the hardening process of Co28Cr6Mo specimens are not exactly in the most superficial area as desired, presenting maximum values in the subsurface. The location of these plastic deformations is directly related to the location of the maximum shear stresses.

HertzWin software is based on an elastic linear contact model; however, it can be used to discriminate the influence of variables. This software allows, among other things, to evaluate the depth and location of the maximum shear stresses according to i) the characteristics of the materials in contact (respective Young modulus and Poisson ratios) and ii) the values of the normal force and the coefficient of friction. In this case, two crossed cylinders were considered in order to evaluate this depth (a Co28Cr6Mo cylinder in contact with a tungsten carbide cylinder, simulating the mechanical tests conditions). As

the maximum plastic deformations are equally found in these locations, this software reinforces the conclusion that, in fact, for the hardening conditions in question, it was not possible to obtain this hardening in a strictly superficial way, as would be desired.

Figure 5.9, Figure 5.10 and Figure 5.11 represent, respectively, the locations of the maximum shear stresses for Mechanical Test 2 (normal force of 19.79 N and coefficient of friction 0.221), Mechanical Test 3 (normal force of 10.57 N and coefficient of friction 0.147) and Mechanical Test 4 (normal force of 5.93 N and coefficient of friction 0.145). Note that the surface of the samples is at the upper end of each image.

Figure 5.9. Location of maximum shear stress for Mechanical Test 2 (normal force of 19.79N and coefficient of friction 0.221), in dark red.
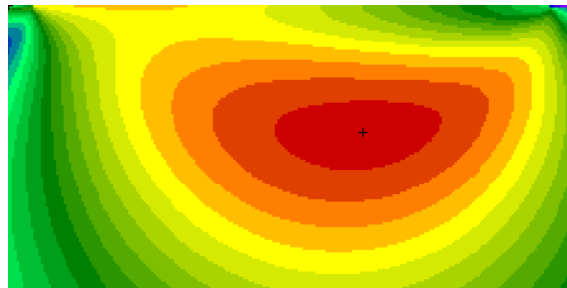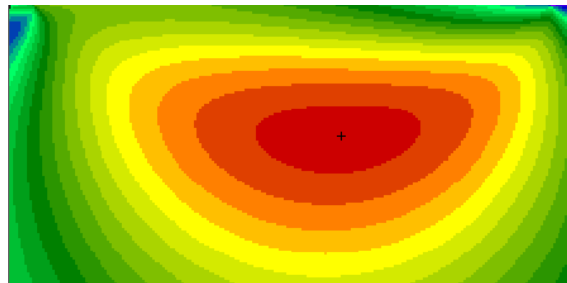

Figure 5.10. Location of maximum shear stress for Mechanical Test 3 (normal force of 10.57N and coefficient of friction 0.147), in dark red.
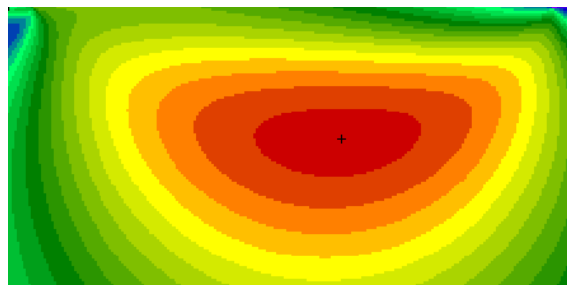

Figure 5.11. Location of maximum shear stress for Mechanical Test 4 (normal force of 5.93N and coefficient of friction 0.145), in dark red.

As can be seen, the maximum values of the shear stresses do not occur at the

surface, for the conditions of the mechanical tests carried out. Thus, it is verified once again that the maximum plastic deformations do not occur, in the same way, at the surface. HertzWin software also allowed to quantify the approximate depths at which the maximum shear stresses occurred, for each mechanical test, as shown in Table 5.1.

Table 5.1. Maximum shear stress depth obtained through HertzWin software, for each mechanical test

Mechanical Test	2 Normal force 19.79 N CoF 0.221	3 Normal force 10.57 N CoF 0.147	4 Normal force 5.93 N CoF 0.145
Maximun shear stress depth [μm]	26.3	22.2	18.3

One of the preponderant factors that makes the zone of maximum shear stress to displace is the coefficient of friction. By analysing these images, it is possible to verify that the coefficient of friction values in question for the three mechanical tests were not high enough to cause considerable deformations on the surface of the Co28Cr6Mo specimens. Using again the HertzWin software, it was verified that a maximum of shear stress occurs in the most superficial zone for a minimum coefficient of friction value of 0.4, as shown in Figure 5.12. This representation is very similar for any value of normal force between 5 and 20 N, so that once again it shows the great influence of the coefficient of friction.
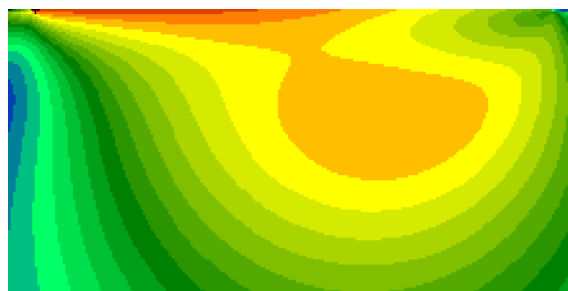
Figure 5.12. Location of maximum shear stress for a coefficient of friction of 0.4. Although this picture was taken for a normal force of 10N, loads of 5N or 20N produce a very similar image.

As an important note regarding this analysis, it is important to mention that the fact that the mechanical hardening tests performed were not associated with values of coefficient of friction high enough for hardening in the most superficial layer possible of the Co28Cr6Mo specimens does not indicate that they were performed under less accurate conditions. In fact, the only variable that could be minimally controlled, indirectly through

its relation with the voltage, evident in Equation 4.1 and Equation 4.2 from Section 4.3.2 (pg. 31), was the normal force applied between the WC and the Co28Cr6Mo cylinder during hardening on the lathe. The coefficient of friction is one of the dependent variables, i.e., it was not possible to control or estimate initially its approximate value.

Finally, the use of this software allows conclusions to be drawn regarding the numerical model and the hardness profile initially created. As mentioned in Section 5.1.3 (pg. 47), a reduced resolution of the hardness profile, 50 μm between indentations, was taken into account. This resolution is insufficient to highlight the areas associated to the maximun shear stress depth of the samples related to the different mechanical tests (Table 5.1). Likewise, the numerical model proves to be insufficient. The numerical model showed an increase of the hardness up to 80 μm below the surface, as seen in Section 5.1.1 (pg. 43). Although the mesh has been refined near the surface, its dimension is still not fine enough to discriminate the shear stress variation field, i.e., the resolution is not adequate to perform the desired analysis. The mesh from Figure 5.1 in Section 5.1.1 (pg. 43) reveals distances of about 20 μm between nodes. Thus, the created numerical model proves to have a precision below the required value.

5.2. Wear and friction behaviour

5.2.1. Friction behaviour

As said above in Section 4.3.5 (pg. 36), the tribological tests performed allowed not only to quantify the final wear but also the average frictional force and therefore coefficient of friction from each test. The mean values were obtained from the respective instantaneous values recorded throughout every test. These values can be seen in Table 5.2.

Table 5.2. Average coefficient of friction values obtained during each tribological test, for the untreated sample and for each of the three treated samples.

	Untreated	Mechanical Test 2 Normal force 19.79N CoF 0.221	Mechanical Test 3 Normal force 10.57N CoF 0.147	Mechanical Test 4 Normal force 5.93N CoF 0.145
1N	0.3878	0.5254	0.4951	
2N	0.3343	0.3805	0.4705	
4N	0.3701	0.5200	0.3173	0.3171
6N	0.4701	0.5815	0.3839	
8N	0.6187	0.5004	0.3957	0.5507
10N	0.3923	0.3858	0.3990	0.3969
12N	0.4907	0.3553	0.4840	0.5359

Note: it was not possible to obtain these values for 1, 2 and 6 N forces from tribological tests associated with the Co28Cr6Mo sample treated during Mechanical Test 4.

The analysis of the instantaneous friction evolution becomes relevant since there are evolutions typical of an abrasive process and evolutions typical of a situation of high formation and fixation of oxides on the surface subject to wear. By identifying the graphical representations as clear situations of abrasion or oxide formation, it is possible to validate that certain wear marks obtained in the tribological tests correspond mostly to one or the other case. This analysis will be reinforced further in Section 5.2.3.2 (pg. 64).

Blau (1996) identified common shapes of friction-time curves based on a survey of the tribology literature, in the early 1980s. Although the causes for different shapes are not uniquely connected to a single set of cooperative mechanisms (the shape of a friction-time curve is affected not only by the materials involved but also by the applied load and other tribosystem characteristics), it is possible to distinguish abrasive situations from major oxide formation situations. These two typical cases are shown, respectively, in Figure 5.13 and Figure 5.14.
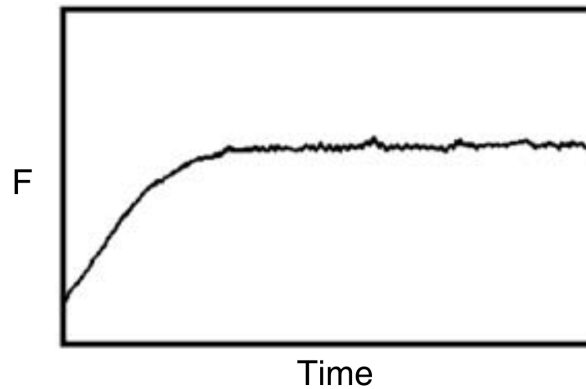
Figure 5.13. Typical abrasive situation friction-time curve (Blau,1996).
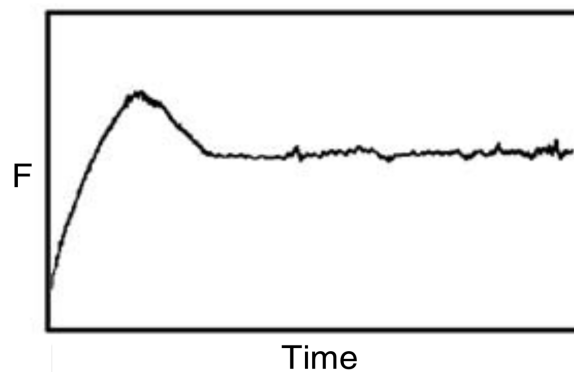
Figure 5.14. Typical friction-time curve from a situation with high formation and fixation of oxides in the wear surface (Blau,1996).

Taking into account the typical evolution of each case mentioned, it was possible to make a comparison with the evolutions registered during the tribological tests.

It is important to identify pure abrasion situations from high oxide setting situations. Thus, this comparison between Blau (1996) friction-time curves, and friction-time curves obtained during the experimental works of this investigation is relevant to allow this validation and distinction between the two situations. Thus, taking the 8 N normal force tribological test associated to the untreated Co28Cr6Mo sample, represented in Figure 5.15, high similarities with Figure 5.13, associated to an abrasive wear process, can be verified.
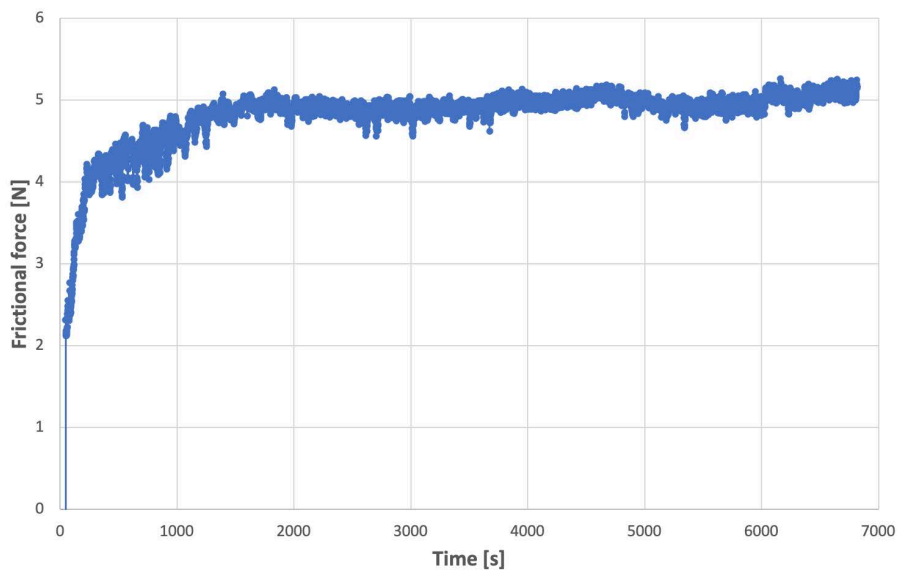
Figure 5.15. Friction-time curve for the 8N normal force tribological test with the untreated specimen.

In addition to the validation made for abrasive wear cases, it is important to make the analogous analysis for situations where there was a high fixation of oxides. Figure 5.16 represents the evolution of the instantaneous frictional force (i.e. the friction-time curve) for the tribological test of 10 N performed on the specimen related to the Mechanical Test 3 (normal force of 10.57 N and coefficient of friction 0.147). As can be seen, there are strong similarities between this representation and Figure 5.14, validating that, in fact, under these conditions, the formation and fixation of an oxide layer occurred on the wear surface, which promoted a reduced amount of removed material, that is, a smaller volume of Co28Cr6Mo removed from the surface of this cylindrical specimen.
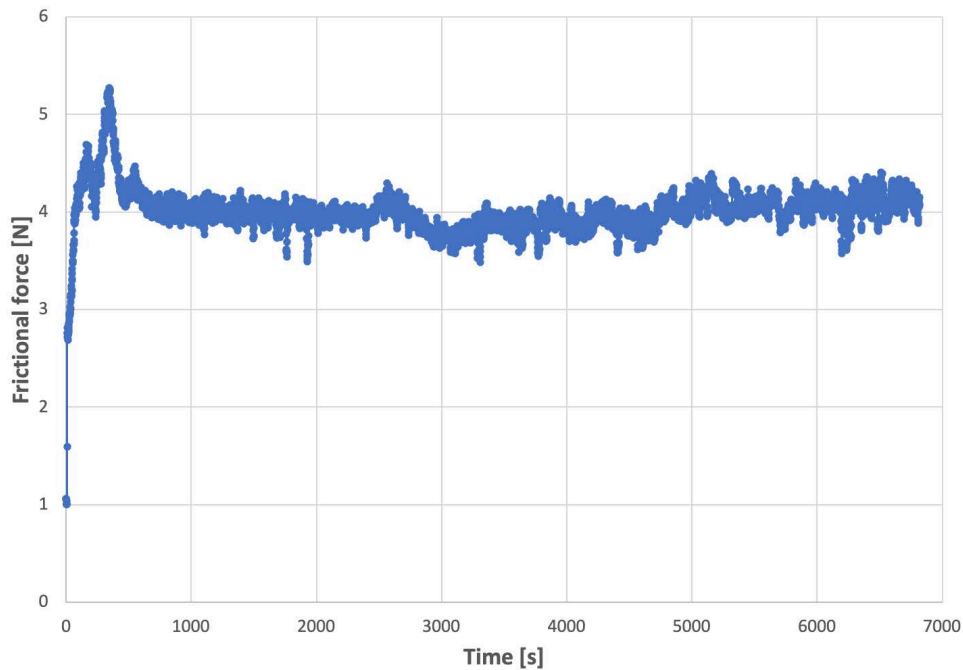
Figure 5.16. Friction-time curve for the 10N normal force tribological test with the Mechanical Test 3 (normal force of 10.57N and coefficient of friction 0.147) specimen.

5.2.2. Wear behaviour

As said before, the tribological tests quantified the final wear and the coefficient of friction throughout the tests. They allowed further analysis of the volume of material removed from the Co28Cr6Mo cylinder (note again that these tests were carried out for an untreated sample and the three cold-worked samples subjected to 5.93, 10.57 and 19.79 N normal force applied). They also allowed the determination of the wear coefficient k, an important variable to make wear quantifiable.

Figure 5.17 depicts a comparative graph of the removed volume from the samples, V(x'), both for the untreated sample and for the mechanical tests. It is important to recall that values from both V(x') and x' were determined by using the formulas from Equation 4.4 to Equation 4.11, in Section 4.3.5.1 (pg. 37). This graph allowed to quantify the removed volume of Co28Cr6Mo material with the product of the normal force by the sliding distance, applied to each specimen, for each tribological test. It is important to emphasize again that the normal force values used for each sample were 1 N, 2 N, 4 N, 6 N, 8 N, 10 N and 12 N.

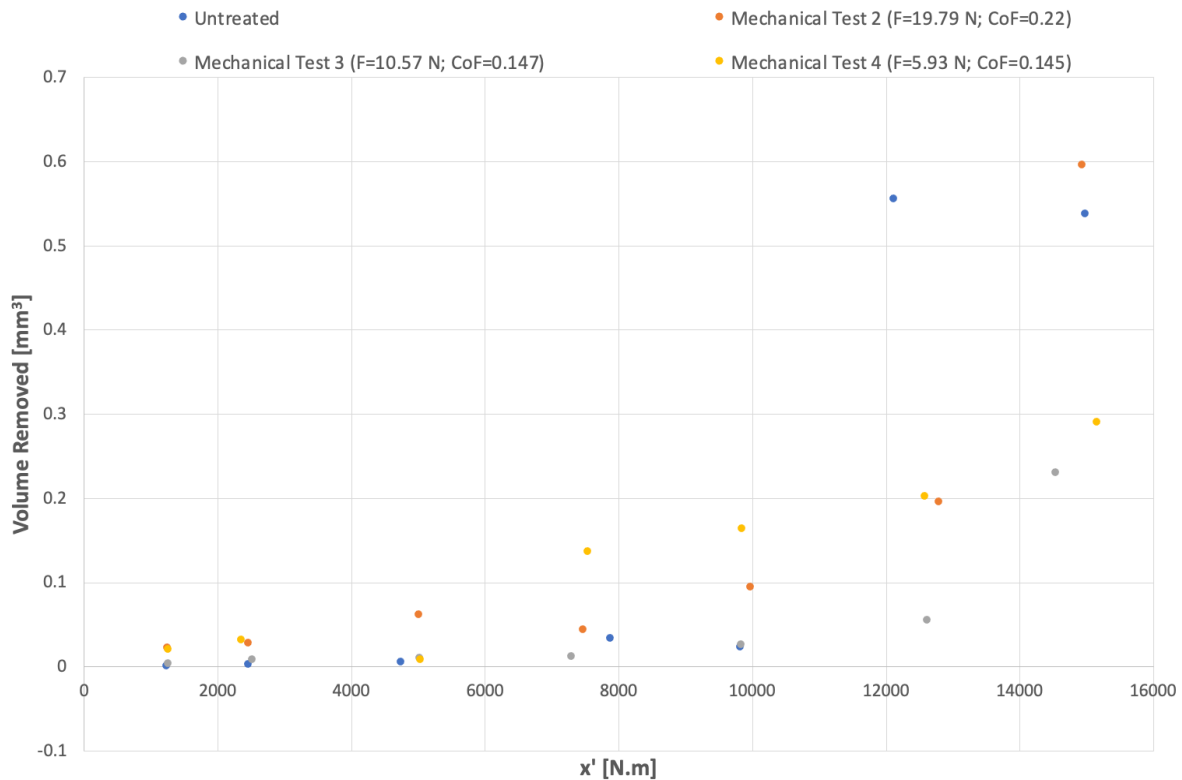Figure 5.17. Evolution of the wear volume with the product between the applied load and sliding distance for Co28Cr6Mo samples (normal force applied: 1, 2, 4, 6, 8, 10 and 12 N).

The analysis of Figure 5.17 allows us to draw some important conclusions. Preliminarily, although the V(x') graph does not directly reveal the applied normal force values, it is possible to visualize them. An initial analysis identifies clusters of four points each, belonging to the mechanical tests and to the untreated sample. There are seven clusters of these in total, which, along the abscissa axis, are associated, respectively, with the 1 N, 2 N, 4 N, 6 N, 8 N, 10 N and 12 N tribological tests. This initial conclusion allows the necessary reasoning to critically analyse the removed volume evolutions for each case.

Through Figure 5.17, it is possible to observe that there are intervals between certain normal force values in which there is a very significant increase in the removed Co28Cr6Mo material: for the untreated sample, this increase occurs for a normal force of 10 N, while for the test in which a normal force of 19.79 N was applied (Mechanical Test 2) it occurs for a normal force of 12 N. Regarding the tests in which normal forces of 10.57 and 5.93 N were applied (Mechanical Tests 3 and 4 respectively), there is no marked transition. This sudden increase in removed material is highly undesirable, since the objective of the cold surface hardening previously carried out would be to improve the mechanical properties of this alloy, that is, mainly to reduce the wear it would be subjected to when in

service (e.g., in the human body, since Co28Cr6Mo is an alloy used for biomedical applications).

From Figure 5.17 it is possible to make another, equally relevant analysis. The results associated with the test in which a normal force of 19.79 N was applied (Mechanical Test 2) show that, for 12 N, the volume of material removed during tribological testing is greater than the volume of material removed for the untreated cylindrical specimen. This goes completely against the objective of the cold hardening performed earlier. Note that this mechanical test has the highest value of normal force applied during the hardening process compared to the other two tests, between the Co28Cr6Mo cylinder and the WC cylinder. This fact, together with the evolution of the volume of material removed, led to the conclusion that the normal force applied in the mechanical treatment prior to the tribological tests of the cylinder of Mechanical Test 2 was excessive, which caused an exaggerated deformation of the grains of this alloy; thus, instead of obtaining an improvement of the mechanical properties, the opposite happened, with their degradation. However, this may not be the unique justification, as will be proven below in Section 5.2.3.1 (pg. 68), with the specific analysis of the possible formation of oxides in the wear marks of this mechanical test specimen in comparison with others.

In addition to this graphical analysis of Figure 5.17, it is important to quantify the wear obtained for each tribological test of each Co28Cr6Mo sample. For this, k (i.e. the wear coefficient) was calculated for each of the cases. As mentioned above, this variable represents the slope of a linear relationship associated with the progression of V(x'). More specifically, each value of k associated with a certain point, corresponds to the slope of the line formed between this point and the origin of the referential. This calculation was possible using the expressions presented above in Section 4.3.5.1 (pg. 37). Table 5.3 represents the wear coefficient values for each tribological test performed on each of the Co28Cr6Mo samples (one untreated sample and 3 samples subjected to different treatment conditions associated with mechanical tests 2, 3 and 4).

Table 5.3. Wear coefficient (k) values for each tribological test performed on each Co28Cr6Mo sample.

×10⁻⁶	Untreated	Mechanical Test 2 Normal force 19.79N CoF 0.221	Mechanical Test 3 Normal force 10.57N CoF 0.147	Mechanical Test 4 Normal force 5.93N CoF 0.145
1N	1.3221	18.7332	2.9231	16.8888
2N	1.1909	11.5297	3.3100	13.6497
4N	2.3789	12.4807	2.2096	1.7467
6N	4.3659	5.9697	1.7001	18.1645
8N	2.3789	9.5444	2.7103	16.7151
10N	45.9266	15.3279	4.3942	16.1465
12N	35.9505	39.9207	15.8712	19.1678

Note: values of k are multiplied by 10⁻⁶, as stated in the first cell of the table.

Table 5.3 makes it possible not only to reconclude that, in fact, there are values of normal force applied in the tribological tests of certain Co28Cr6Mo samples that lead to a very sharp increase in the volume of material removed, but also it makes it possible to quantify this increase, using the wear coefficient k. For the untreated sample, this increase occurs for a normal force of 10 N, as analysed above. It can be seen from this new analysis that the value of k increases by about 19.3 times compared to the 8 N tribological test of the same sample, which is consistent with what was concluded from Figure 5.17. Not only is this true but also this value is 3, 10.5 and 2.8 times higher than the analogous k values of Mechanical Tests 2, 3 and 4, respectively. Furthermore, the k value of the 12 N tribological test, associated with the Mechanical Test 2 sample (19.79 N normal force and coefficient of friction 0.221), is visibly high, being identical to the analogous value of the untreated sample but far superior than the values of the Mechanical Tests 3 and 4 samples (2.5 and 2.1 times, respectively). Thus, once again, a transient regime of volume removed of Co28Cr6Mo is observed for the untreated and Mechanical Test 2 samples, while this is not the case for the samples of Mechanical Tests 3 and 4. Finally, it is important to note that,

for the two highest values of normal force applied during the tribological tests (10 and 12 N), the sample associated with Mechanical Test 3 (10.57 N normal force and coefficient of friction 0.147) is the one that notably reveals the lowest values of wear coefficient, k. This reveals a visible better wear behaviour of this alloy when subjected to these hardening conditions.

With these analyses, it is initially possible to conclude that Mechanical Tests 3 and 4 (once again, related to normal forces of 10.57 and 5.93 N respectively) are beneficial at this point: for the normal force studied values they do not reveal any sudden transition to very high material removal values. Furthermore, Mechanical Test 3 (10.57 N normal force and coefficient of friction 0.147) reveals the lowest values of coefficient of wear, especially for the highest normal forces applied during the tribological tests, also distinguishing itself positively from Mechanical Test 4 (5.93 N normal force and coefficient of friction 0.145).

5.2.3. Wear Mechanisms

5.2.3.1. SEM and Microscope Analysis of the Possible Formation of Oxides in the Samples' Wear Marks

As previously mentioned, the tribological tests aimed to analyse the wear behaviour not only of the treated specimens (mechanical tests 2, 3 and 4) but also of an untreated specimen, through the removed volume of Co28Cr6Mo. Throughout each tribological test, concave and elliptical wear marks were created, associated with this removal of material represented schematically above, in Figure 4.17 from Section 4.3.5.2 (pg. 39). As analysed above, there were certain values of normal force applied in the tribological tests on the specimens associated with certain mechanical tests and the untreated specimen that caused a very sharp transition in the volume of material removed from the alloy under analysis: the need arose to seek a justification for this exaggerated increase.

It was decided to analyse the possible formation of oxides in the wear marks; these oxides, being typically much more rigid than the initial material that formed them, could constitute a protective layer against wear, justifying the mechanical tests in which an accentuated transition in the volume of material removed was not observed. The higher the density of these oxides on the surface of the wear marks, the lower the associated removed volume and consequently the greater the protection conferred to this Co28Cr6Mo alloy. It should be emphasised that, tendentially, these oxides would only form for relatively low

values of applied normal force. This is due to the fact that, with the increase of the normal force, there is a consequent increase of the tangential forces that hinder the formation of oxides in the areas subject to wear. However, this fact will not affect the possible fixation of oxides for the tribological tests in question, since the maximum normal force applied on these (12 N) is a low value.

Thus, SEM was used to verify the existence of oxides and quantify it. As previously mentioned, a SEM builds images of a determined sample by scanning its surface with a focused beam of electrons. These electrons interact with atoms in the sample surface, producing various signals that contain information not only about the surface topography but also about the composition of the sample. Therefore, this equipment was useful not only to visualise possible oxides formed but also to prove that they were indeed oxides, through an analysis of their chemical composition. Detailed reports were carried out that made available this chemical composition, from different zones under analysis. As can be seen in the Figure 5.18, a line was drawn over a certain dark spot, in this case, relatively to the sample of the mechanical test in which a normal load of 19.79 N was applied, when subjected to 12 N in the tribological test.
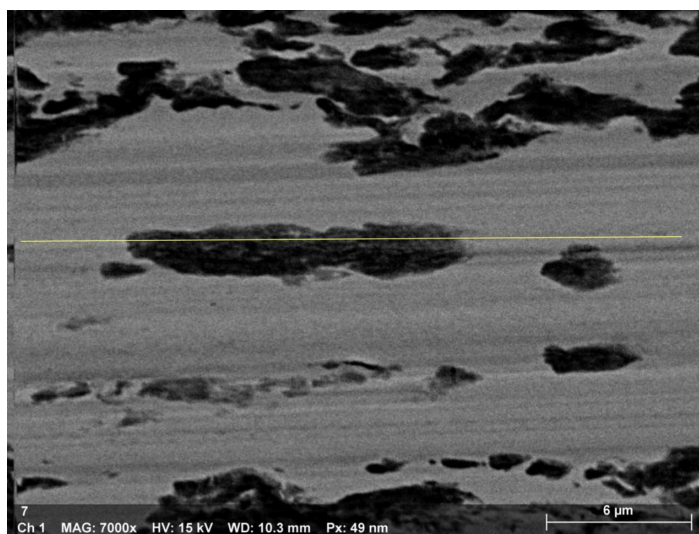

Figure 5.18. Line that will serve as a marker over the zone to be analysed in terms of chemical composition. This feature is one of the strengths of an analysis using a SEM.

If a high concentration of oxygen (O) is found in the area to be analysed, it is confirmed that this is an area of deposited oxides on the wear mark. Table 5.4 shows the detailed chemical constitution of this area, which is part of the SEM report. As can be seen, there is a high atomic oxygen concentration in this area (21.75%) validating the hypothesis that the dark marks involved correspond to oxides.

Table 5.4. Chemical composition of the line analysed by SEM.

Element	At. No.	Netto	Mass [%]	Mass Norm. [%]	Atom [%]	abs. error [%] (1 sigma)	rel. error [%] (1 sigma)
Co	27	36063	50.79	55.66	43.54	1.57	3.09
Cr	24	36931	26.93	29.51	26.16	0.81	3.02
O	8	10299	6.89	7.55	21.75	0.99	14.30
Mo	42	10598	5.27	5.77	2.77	0.22	4.19
C	6	754	1.37	1.50	5.76	0.36	26.40
			Sum 91.24	**100.00**	**100.00**		

Making a comparative analysis of a zone with a low concentration of oxides, such as the one in Figure 5.19, it can be seen that the amount of oxygen is lower when compared to the previous analysis. Table 5.5 shows the chemical composition for this case, revealing a substantially lower atomic concentration of this element (1.78%). This is a form of comparison to verify once again that, in fact, the dark areas correspond to clusters of oxides. This result is consistent with the initial hypothesis formulated since the line drawn for this case overlaps with light areas, without many dark marks that would correspond to potential oxide formations.
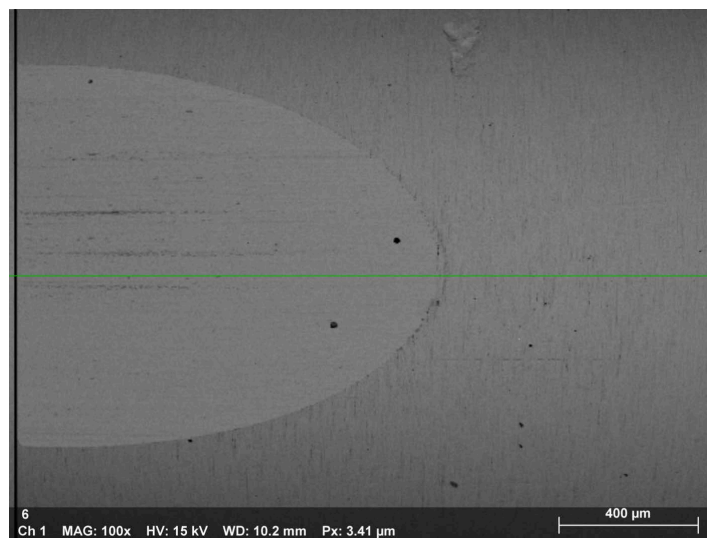

Figure 5.19. Line that will serve as a marker over the zone to be analysed in terms of chemical composition. This time it covers a relatively large area with a low percentage of black marks.
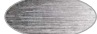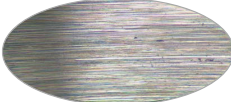
Table 5.5. Chemical composition of the line analysed by SEM.

Element	At. No.	Netto	Mass [%]	Mass Norm. [%]	Atom [%]	abs. error [%] (1 sigma)	rel. error [%] (1 sigma)
Co	27	22741	59.55	63.30	56.79	1.86	3.12
Cr	24	19599	26.57	28.24	28.72	0.82	3.08
Mo	42	6230	5.41	5.75	3.17	0.23	4.32
C	6	579	2.04	2.17	9.54	0.57	27.86
O	8	387	0.51	0.54	1.78	0.18	35.26
		Sum	94.07	100.00	100.00		

5.2.3.2. Oxide fixation on wear marks

It is important to have an overview of the wear marks created during the tribological tests on the various Co28Cr6Mo specimens, for all values of normal force applied. Thus, Table 5.6 represents the photographs of all these marks taken with the optical microscope, where the area of the ellipse was cropped. It is important to recall the relative position of the wear marks with respect to the Co28Cr6Mo samples, shown above in Section 4.3.5.2 (pg. 39), Figure 4.17. Through this general analysis it is possible to observe the differences in oxide concentration fixed between samples from different mechanical tests (in other words, between samples with different initial hardening conditions) for different values of normal force applied during tribological tests (table rows). Additionally, and since the images are all at the same scale, it is possible to observe the variation of their size with the increase of the normal force applied during the tribological tests.

Table 5.6. Wear marks' ellipses for each tribological test performed.

	Untreated	Mechanical Test 2 Normal force 19.79N CoF 0.221	Mechanical Test 3 Normal force 10.57N CoF 0.147	Mechanical Test 4 Normal force 5.93N CoF 0.145
1N				
2N				
4N				
6N				
8N				
10N				
12N				

Note: The images are all at the same scale.

Preliminarily, it is possible to draw some conclusions from the analysis of the

Table 5.6, regarding the size of the ellipses. There is a generic increasing trend of their sizes with the increase of the normal force applied in the tribological tests, which is coherent since the volume of Co28Cr6Mo removed has an increasing tendency with the increase of the applied force. Furthermore, and comparing the different samples, it can be seen, once again, the best behaviour to wear of the specimen relative to Mechanical Test 3 (10.57 N normal force and coefficient of friction 0.147). In fact, there is a smoother progression in the growth of the ellipse size with the increase of the normal force when compared against the other samples. Moreover, the sample of this mechanical test is the one which reveals the smallest ellipse dimensions for the highest values of force in the tribological tests, reinforcing the fact that it shows an optimised behaviour to wear.

In addition to that, it is also interesting to analyse the volume removed as a function of the normal force applied during the tribological tests. A V(F) bar graph allows a better visualisation of the wear behaviour of the specimens from each mechanical test (and the untreated specimen). It also allows to efficiently cross the results obtained from the volume removed with the respective photographs of the wear marks from Table 5.6, understanding the influence of the oxide fixation on the wear that occurred. These two pieces of information, V(F) graph and oxide density photographs, will allow to draw more precise conclusions on the wear behaviour of this Co28Cr6Mo alloy.

By analysing Table 5.6 it is possible to label each tribological test as mostly abrasive or influenced by high oxide attachment and to insert this binary information into a V(F) graph, as shown in Figure 5.20. Each bar with "a" above it represents a tribological test with mainly abrasive wear, and each bar with "o" a test with a high concentration of oxides in the wear mark. At this point we must explicitly differentiate between oxide marks and abrasive marks. There are abrasive marks along the photographs in Table 5.6 that appear to be oxides because of their dark colour. However, this is due to a shadow effect, caused naturally by the lighting conditions when the photographs were taken. It is still possible to distinguish these marks from the oxide marks. The abrasive marks (whether dark or light) have a purely linear shape along the ellipse. On the contrary, the marks associated to the fixation of oxides present variable shapes: black round spots or other irregular shapes but never perfectly linear shapes (typical of abrasion). Thus, it is possible to make this distinction.

Furthermore, it is important to cross-check this information with what has been previously validated, in Section 5.2.1 (pg. 53). The exemplifying tribological tests in that

section whose friction-time curves correspond to typical progressions of abrasive situations and oxide fixation situations correspond to photographs in Table 5.6, in which purely abrasive wear marks and marks with high oxide concentration are also evident, respectively. This combination of reasoning reinforces the validity of these two mechanisms associated to the wear marks on Co28Cr6Mo samples.

Note: "a" indicates a wear mechanism mostly abrasive;
"o" indicates the significant concentration of oxides on the surface of the wear mark.
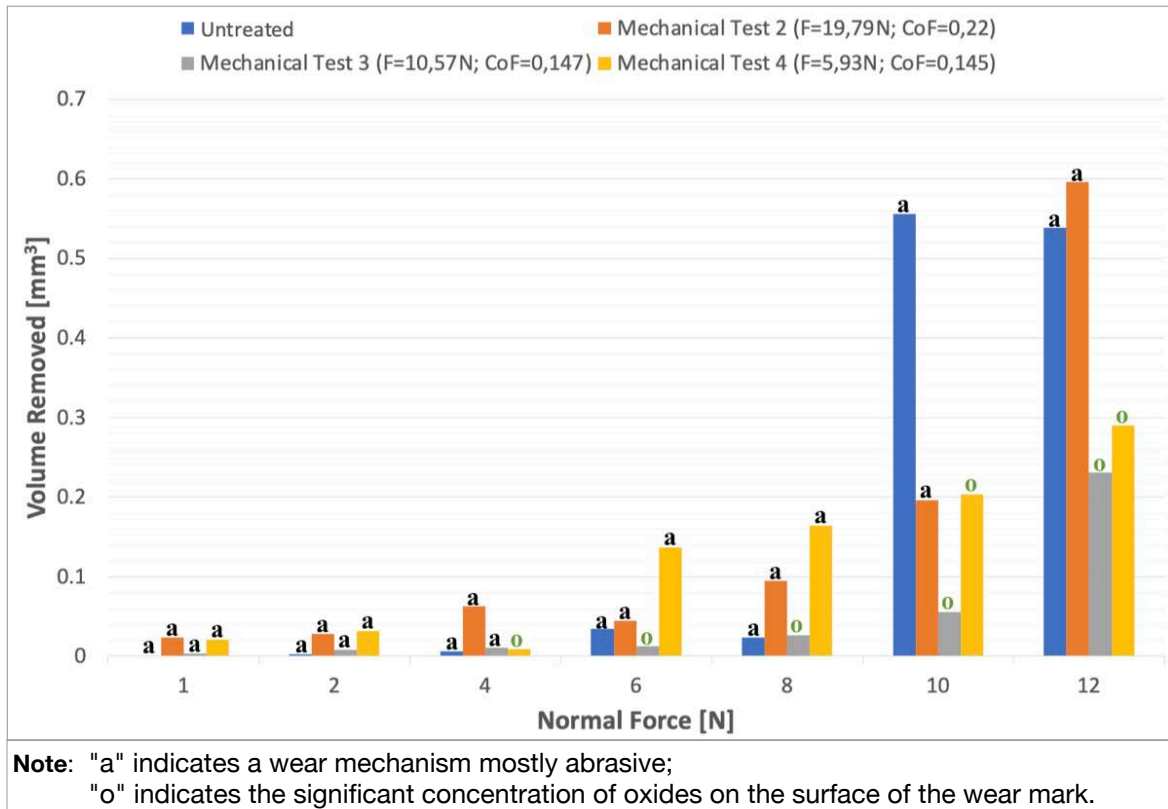
Figure 5.20. Evolution of the volume of Co28Cr6Mo removed during the tribological tests, for each normal force applied. Comparative analysis between the specimens previously hardened in different conditions and between these and the untreated specimen.

Through the analysis of Figure 5.20 it is possible to draw some conclusions related to the comparative evolution of the volume of Co28Cr6Mo removed with the increase of normal force applied in the tribological tests, better explained below in Section 6 (pg. 77):

- Oxidation is prevailing for the highest applied normal forces, mainly for Mechanical Test 3 (associated to a normal force applied during its hardening of 10.57 N and a coefficient of friction of 0.147) and Mechanical Test 4 (associated to a normal force applied during its hardening of 5.93 N and a coefficient of friction of 0.145).
- For higher normal force values, tribological tests whose marks show significant abrasive wear are associated with a much higher removed material volume than tests whose marks have high fixation of oxides.

- The specimen of Mechanical Test 3 (associated to a normal force applied during its hardening of 10.57 N and a coefficient of friction of 0.147) reveals much more adequate wear values for higher forces applied in the tribological tests, when compared to the other test specimens. This reveals that, for the largest domain of forces involved in the mechanical wear of a component of this alloy in the human body, a mechanical treatment performed under the conditions of this mechanical test proves to be the closest to an optimal situation.

5.2.3.2.1. Oxide formation on wear marks specific comparisons

Adopting the previous reasoning in Section 5.2.3.1 (pg. 61) regarding the formation of oxides, it is understandable that, for example, the wear marks on the Co28Cr6Mo specimen from the test in which a load of 10.57 N was applied (Mechanical Test 3) have a higher density of oxides on their surface than the wear marks associated with the test in which a load of 19.79 N was applied (Mechanical Test 2), mainly for higher normal force values in tribological tests. This is due to the fact that the specimen from Mechanical Test 3 shows much lower volumes of removed material than the specimen from Mechanical Test 2 as seen above, in Figure 5.20 from Section 5.2.3.2 (pg. 64); furthermore, Mechanical Test 2 shows a very sharp transition in volume of removed Co28Cr6Mo for a normal force of 12 N, which is not the case at all for Mechanical Test 3. Figure 5.21 and Figure 5.22 represent SEM analysis of the wear marks created on the samples associated to Mechanical Test 2 and Mechanical Test 3 respectively (both for a normal force of 12 N, applied during the tribological test). This visualisation through SEM allows a more accurate comparative analysis of particular cases than that obtained above through microscopy, in Figure 5.20.

Figure 5.21. Visualisation in SEM of the wear mark from the test in which a load of 19.79N was applied (Mechanical Test 2) associated to a normal force of 12N in the tribological tests.
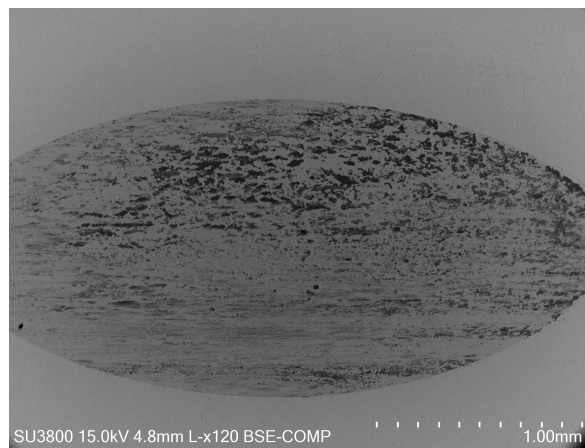
Figure 5.22. Visualisation in SEM of the wear mark from the test in which a load of 10.57N was applied (Mechanical Test 3) associated to a normal force of 12N in the tribological tests.

As referred to before, the oxides visualised in the SEM analysis are the dark spots. This was already proven by checking the chemical composition of these spots: Figure 5.4 and Figure 5.5 from Section 5.2.3.1 (pg. 61). It is possible to verify that Figure 5.21 and Figure 5.22 are coherent with what would be expected at first: the wear mark associated to Figure 5.21 presents a much lower density of oxides when compared to the analogous wear mark of Figure 5.22. Thus, the marked transition in removed volume between the 10 N and 12 N tribological tests of the test in which a normal force of 19.79 N was applied (Mechanical Test 2) is again justified (note that it has already been partially justified by the excessive grain deformation associated with this test; the normal force applied during cold-hardening was too great). On the other hand, the higher density of oxides at the surface of the wear mark associated to the test in which a normal force of 10.57 N was applied (Mechanical Test 3) explains the inexistence of a removed volume transition of Co28Cr6Mo

for the normal force values used: the fixation of a considerable amount of oxides allowed the constitution of a protective layer against wear.

In addition to this comparative analysis it is possible to make others in order to reinforce this influence of the existence of oxides on the surface of the wear marks on the volume of material removed. Through Figure 5.20 from Section 5.2.3.2 (pg. 64) it is possible to verify that, for a normal force of 10 N, the untreated sample and the sample from Mechanical Test 3 (associated to 10.57 N of normal force and coefficient of friction 0.147) present very different values of removed volume, revealing a very different behaviour to wear. In fact, this last sample presents much lower values than the untreated one (approximately 10 times lower). Figure 5.23 and Figure 5.24 represent the wear marks corresponding to these samples, visualized in the optical microscope.
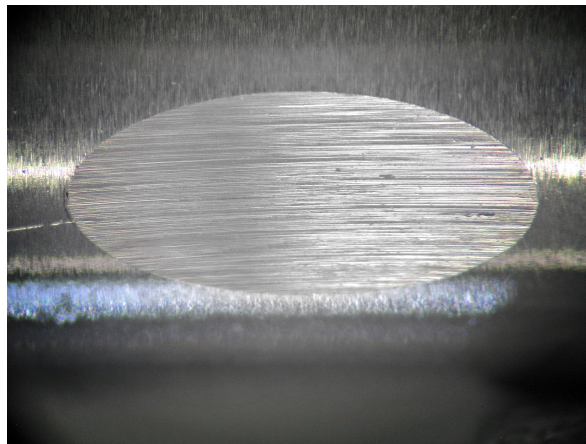
Figure 5.23. Visualisation in the optical microscope of the wear mark from the untreated sample associated to a normal force of 10N in the tribological tests.
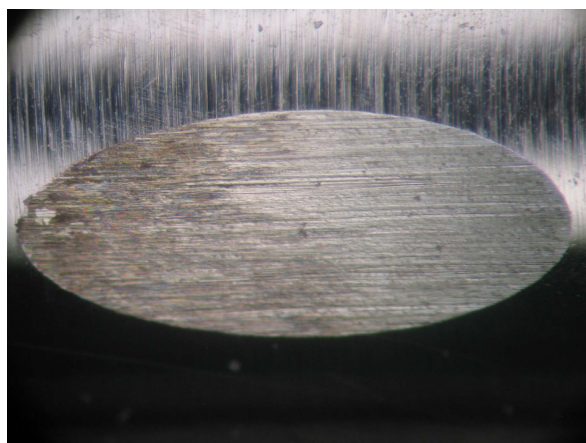
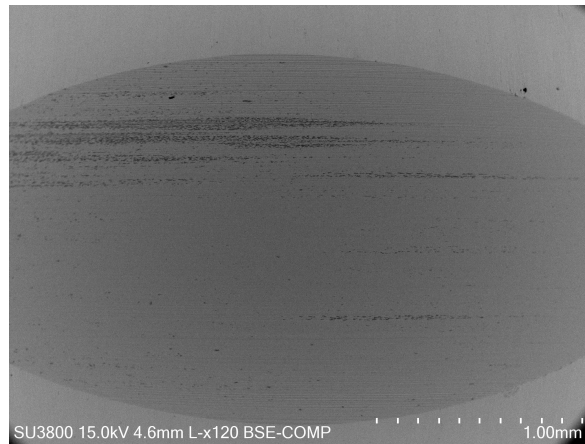Figure 5.24. Visualisation in the optical microscope of the wear mark from the test in which a load of 10.57N was applied (Mechanical Test 3) associated to a normal force of 10N in the tribological tests.

The difference in oxide density between these two samples for 10 N can be ob-

served. In Figure 5.23, the oxides are practically non-existent, manifesting themselves in punctual and very small agglomerations. On the contrary, in Figure 5.24, associated to Mechanical Test 3 (10.57 N of normal force applied and coefficient of friction 0.147), there is a much higher density of oxides: more than half of the wear mark surface is covered by them. Again, this indicates the influence of oxide attachment on the wear behaviour of this cobalt alloy; its increased concentration is associated with a lower volume of Co28Cr6Mo removed.

5.2.3.3. Oxide fixation on zirconia rings

As mentioned above in Section 4.3.5.3 (pg. 41) the analysis of the oxide formation on the wear marks of the specimens can be supported with the analysis of the oxide concentration on the zirconia rings' traces, during the tribological tests. Wear marks with high concentration of oxides can be expected to be associated with traces on the zirconia ring with abundant oxides as well. Figure 5.25 shows the magnified view of a wear track of the zirconia ring associated to the 10 N tribological test performed on the Mechanical Test 3 (normal force of 10.57 N and coefficient of friction 0.147) specimen.
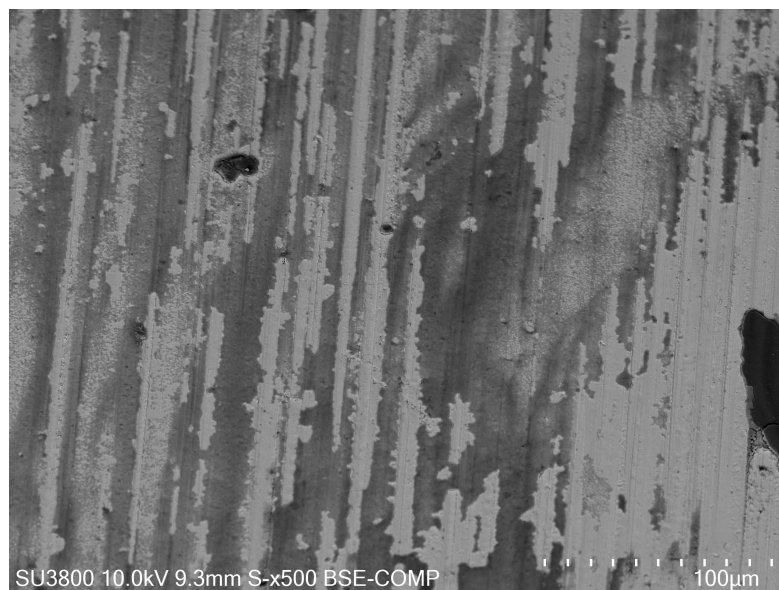
Figure 5.25. Black marks on the zirconia ring associated to the 10N normal force tribological test for the specimen hardened in Mechanical Test 3 (normal force of 10.57N and coefficient of friction 0.147).

As can be seen, there is a high density of black spots. It would be consistent that these spots were oxides: the wear surface on the Co28Cr6Mo sample associated with this particular tribological test has demonstrably high oxide fixation. This can be analysed through the image corresponding to this case in Table 5.6 and the volume removed of ma-

terial shown in Figure 5.20 (as this volume presents a very low value in relation to the other samples, it reinforces the fact that these black spots are oxides), both from Section 5.2.3.2 (pg. 64). Recall that it has been proven that the analysed black spots of the wear marks in the samples are effectively oxides, through SEM analysis in Section 5.2.3.1 (pg. 61).

With regard to Figure 5.25, in order to prove that these zirconia ring tracks have a high amount of oxides, a SEM analysis analogous to that carried out for the wear marks of the samples was performed for this ring. After magnifying one of the black spots from Figure 5.25, the area of material whose chemical composition was going to be quantified was delimited by a green square, as shown in the Figure 5.26.
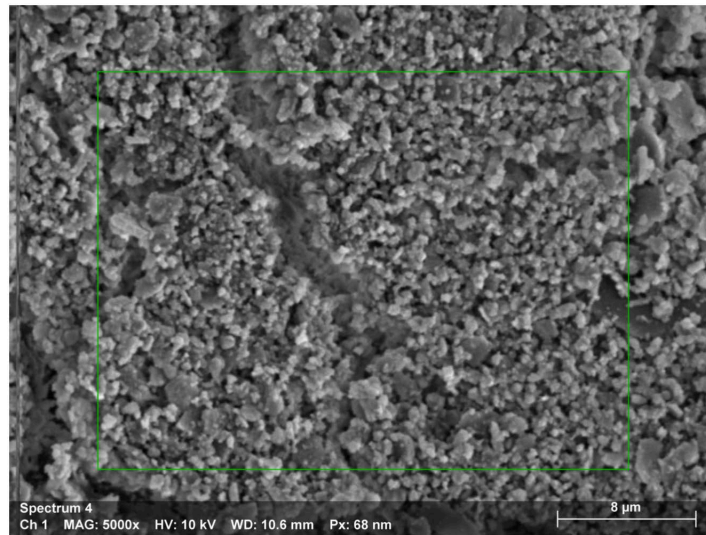
Figure 5.26. Magnification of one of the black spots from the zirconia ring associated to a 10N normal force tribological test on the Mechanical Test 3 sample, ready to be chemically analysed.

Table 5.7 represents the results obtained in the respective report. As can be seen, in atomic composition, 56.08% of the area analysed has oxygen in its constitution, an essential constituent in oxides. This high concentration of this element proves that, once again, the black spots are oxides, this time in the wear track of the zirconia ring.

Table 5.7. Chemical composition of the area of the zirconia ring associated to a 10N normal force tribological test on the Mechanical Test 3 sample.

Element	At. No.	Netto	Mass [%]	Mass Norm. [%]	Atom [%]	abs. error [%] (1 sigma)	rel. error [%] (1 sigma)
Co	27	6472	13.35	31.99	19.41	2.02	15.16
Cr	24	2025	11.26	26.99	18.57	0.55	4.92
O	8	6655	10.47	25.09	56.08	1.58	15.14
Mo	42	4267	6.64	15.93	5.94	0.29	4.43
		Sum	**41.72**	**100.00**	**100.00**		

After validating the existence of oxides on the surface of the zirconia ring, it is possible to associate a wear track to each tribological test performed, analogously to what was done above in Table 5.6, from Section 5.2.3.2 (pg. 64). Thus, microscopies of the various rings used for the various tests associated with the different specimens were gathered, as shown in Table 5.8.

Table 5.8. Wear tracks on zirconia ring for each tribological test performed.

	Untreated	Mechanical Test 2 Normal force 19.79N CoF 0.221	Mechanical Test 3 Normal force 10.57N CoF 0.147	Mechanical Test 4 Normal force 5.93N CoF 0.145
1N				
2N				
4N				
6N				
8N				
10N				
12N				

Note: The images are all at the same scale.

As can be seen, there is a visible difference in the concentration of oxides in

the zirconia rings between certain tribological tests. The tests which were previously associated with high oxide concentrations on the surface of the wear marks of the Co28Cr6Mo specimens show an equally high oxide fixation in the corresponding zirconia ring track. More specifically, the specimen associated to Mechanical Test 3 (normal force applied of 10.57 N and a coefficient of friction of 0.147) reveals to be the one with the highest density of these oxides for higher values of normal force applied during the tribological tests. This verification is consistent with what is observed above, not only in Table 5.6 but also in Figure 5.20, Section 5.2.3.2 (pg. 64), where it can be seen that this specimen was the one which presented the best behaviour to wear, due to the high fixation of oxides.

5.2.3.4. Relationship between wear mark depths and the depth of the deformed zones of the Co28Cr6Mo cylindrical samples

In addition to the analysis above, one must consider an additional factor that may have influenced the wear results. As previously mentioned, the hardening obtained in the mechanical tests did not take place in the outermost possible layer of the Co28Cr6Mo cylindrical specimens. It was found that, for the hardening conditions obtained, this hardening occurred in a sub-layer, slightly below the lateral surface of the specimens, as noticed previously in Figure 5.8 from Section 5.1.3.1 (pg. 49) and validated through HertzWin software results in Figure 5.9, Figure 5.10 and Figure 5.11, Section 5.1.3.2 (pg. 50). This may have an influence on the volume of material removed as the material in the topmost layer was not mechanically hardened: it is important to check whether the wear has reached the mechanically hardened zone in all the mechanical tests carried out. Therefore, again using Equation 4.6 from Section 4.3.5.1 (pg. 37), h (the maximum depth of the concavity resulting from wear) was determined for all tribological tests. By comparing the values of h from each tribological test with the depth of the deformed layer obtained previously by the HertzWin software through simulations, it is possible to verify if this wear reached the mechanically hardened zone for every tribological test of all three Co28Cr6Mo samples associated to the mechanical tests performed.

Table 5.9 presents the values of the maximum depth of concavity formed by wear (through material removal), in the Co28Cr6Mo specimens associated to each mechanical test (i.e. to each cold hardening condition to which they were subjected) for each tribological test.

Table 5.9. Maximum depth of concavity caused by material removal during tribological tests, in μm, for the three specimens hardened under distinct conditions during mechanical tests.

	Mechanical Test 2 Normal force 19.79N CoF 0.221	Mechanical Test 3 Normal force 10.57N CoF 0.147	Mechanical Test 4 Normal force 5.93N CoF 0.145
1N	38.4	15.3	36.6
2N	42.4	23.0	45.2
4N	63.0	26.5	23.6
6N	53.2	28.1	93.2
8N	77.8	41.1	102.2
10N	111.6	59.3	113.6
12N	194.6	121.0	135.8
HertzWin reference value	**26.3**	**22.2**	**18.3**

Note: This depth is at the centre of each ellipse created. HertzWin reference values are also in μm.

As can be seen, for practically all the normal force values of the tribological tests, the verified wear entered through the mechanically deformed zone of each specimen (i.e., the wear reached in almost all cases the previously hardened zone). Thus, this allows concluding that there were favourable conditions to evaluate the influence of the 3 hardening conditions evident in this research work. Since the maximum depth of the wear marks obtained after the tribological tests were mostly greater than the depth of the hardened zones of the respective specimens (i.e., they went beyond the hardened subsurface of the Co28Cr6Mo specimens), all the results obtained were not negatively impacted by the fact that the mechanical treatment of the specimens did not take place in the most superficial zone possible (as proven above).

The analysis of Table 5.9 allows for an additional note. It is once again verified that Mechanical Test 3 (normal force of 10.57 N and coefficient of friction 0.147) was the one that allowed a better wear behaviour: the values of maximum depth of wear marks obtained for this case are visibly lower than those obtained for the other mechanical tests. This is extremely noticeable for the whole range of normal forces applied during the tribological tests.

6. CONCLUSIONS

As previously mentioned, the aim of this research work was to identify optimised conditions for the mechanical surface treatment of Co28Cr6Mo alloy in order to improve its mechanical characteristics, namely its wear behaviour. This improvement is essential considering the great applicability of this alloy in the biomedical sector, namely in joint prosthesis (knees, shoulders and hips mainly) which are subject to high and constant mechanical stress. In order to minimize surgical maintenance interventions and increase the patient's quality of life, it is important to seek the improvement of this type of alloys. Therefore, three mechanical hardening tests were performed under different conditions and their behaviour under prolonged wear was evaluated. The results obtained allowed, undoubtedly, to draw some important conclusions.

Through all the procedures carried out and their results it was possible to observe the following conclusions:

- Through a strain hardening assessment, Section 5.1.3 (pg. 47), it was clear that, with the conditions obtained in the mechanical tests, Table 4.3 from Section 4.3.2 (pg. 31), it was possible to induce the hardening of the Co28Cr6Mo specimens. All three samples, subjected to this hardening by Hertz stress field with friction show, an average evolution of their radial hardness higher than that of the untreated sample. Thus, the conditions of the mechanical tests allowed, in the various cases, a hardening. From here on, it was necessary to better quantify this hardening and compare the mechanical tests with each other.

- Through the analysis of Figure 5.8 from Section 5.1.3.1 (pg. 49) it was possible to observe that the hardening did not occur, as intended, in the most superficial zone of the Co28Cr6Mo specimens. The use of the HertzWin software reinforced this conclusion. Furthermore, the software allowed to conclude from which value of the coefficient of friction it is possible to cause the maximum shear stresses at the surface, that is, to cause plastic deformation and consequently hardening in the most peripheral zone of the cylindrical specimens. It was found that this occurs only from coefficients of friction in the order of 0.4: Figure 5.12, Section 5.1.3.2 (pg. 50). As the mechanical hardening tests performed did not lead to coefficient of friction values of that or-

der, but lower as shown in Table 4.3, Section 4.3.2 (pg. 31), it was not possible to cause surface hardening, but at the subsurface.

• Section 5.2.2 (pg. 57) allowed not only the graphical analysis of the evolution of the volume of Co28Cr6Mo removed by wear from the various samples (one untreated and three associated with mechanical tests 2, 3 and 4), Figure 5.17, but also the quantification of wear through calculated values of the wear coefficient k, Table 5.3. It was possible to observe through this joint analysis that Mechanical Tests 3 and 4 (associated to normal forces of 10.57 and 5.93 N respectively) show the best wear behaviour: for the normal force studied values they do not reveal any sudden transition to very high material removal values. This analysis also allowed to note that Mechanical Test 3 (10.57 N normal force and coefficient of friction 0.147) reveals the lowest values of coefficient of wear (as seen in Table 5.3), especially for the two highest normal forces applied during the tribological tests. This accurate quantification allows it to be positively distinguished from Mechanical Test 4 (5.93 N normal force and coefficient of friction 0.145). Thus, this section allows preliminary verification that the sample showing better wear behaviour is the sample treated under the conditions of Mechanical Test 3 (10.57 N normal force and coefficient of friction 0.147).

• The analysis in Section 5.2.3.1 (pg. 61) allowed the conclusion that the black spots present in the wear marks created after tribological tests of certain conditions and for specimens associated with certain mechanical hardening tests, are in fact agglomerations of oxides. To validate the initial hypothesis, a SEM analysis was essential in the atomic quantification of the chemical composition of these black spots.

• Section 5.2.3.2 (pg. 64) allowed to draw the most significant conclusions of this research work:

  • As can be seen in Figure 5.20, oxidation is predominant for the highest applied normal forces. As said before, once these oxides tendentially form for relatively low values of applied normal force, the range of loads used in the tribological tests were not enough to hinder the formation and fixation of the oxides in the areas subject to wear (due to a consequent increase of the tangential forces).

  • For higher normal force values, tribological tests whose marks exhibit mostly abrasive wear were associated with much higher removed material volume values than tests whose marks have high concentrations of oxides. This helped to validate the initial hypothesis that the existence of oxides promotes a protective

layer against wear in this Co28Cr6Mo alloy.

- The mechanical hardening proved to be mostly favourable to the wear behaviour of this material, except for Mechanical Test 2 (associated to a normal force of 19.79 N and coefficient of friction of 0.22). This mechanical test of cold hardening revealed to have conditions already far from the optimum ones to obtain a significant improvement of the mechanical properties of this Co28Cr6Mo alloy. This indicated that the normal force applied was too high, which could be proved by the excessive plastic deformation visualised in Figure 5.8 from Section 5.1.3.1 (pg. 49).

- The specimen of Mechanical Test 3 (associated to a normal force applied during its hardening of 10.57 N and a coefficient of friction of 0.147) showed much more satisfactory wear values for high forces applied in the tribological tests, when compared to the other test specimens. In fact, this was noticeable for normal forces above 6 N, from which there was significant oxide fixation and a large discrepancy between the volume of Co28Cr6Mo removed in this specimen when compared to the untreated, Mechanical Test 2 and Mechanical Test 4 specimens. This information is consistent with the reasoning already presented on the protective influence of oxide attachment on wear surfaces. This showed once again that these oxides promote the abrupt reduction of removed volume. They proved to be directly related to the improved wear behaviour of this alloy.

- The optimised behaviour of the test piece from Mechanical Test 3 could also be analysed by comparing the maximum depth of the wear marks made during the tribological tests, for the samples from different mechanical tests: Table 5.9 from Section 5.2.3.4 (pg. 75). This was an analogous analysis to that carried out using the V(F) graph in Figure 5.20.

Taking into account all the conclusions drawn and cross-referencing the results obtained, it was possible to create a domain of conditions in which the formation and fixation of an oxide layer was significant, delimiting its boundary with the domain of mostly abrasive wear. Figure 6.1 reveals the most favourable set of conditions for the attachment of oxides to the wear marks, in green. As can be seen among the samples of the different mechanical tests, the sample related to Mechanical Test 3 is the one along a greater exten-

sion within the green zone, that is, the zone of oxide formation. This is consistent with what has already been discussed: in fact, the sample associated with this mechanical test was the one with the cold hardening conditions closest to the optimal conditions for a significant improvement of the mechanical properties of this Co28Cr6Mo alloy.
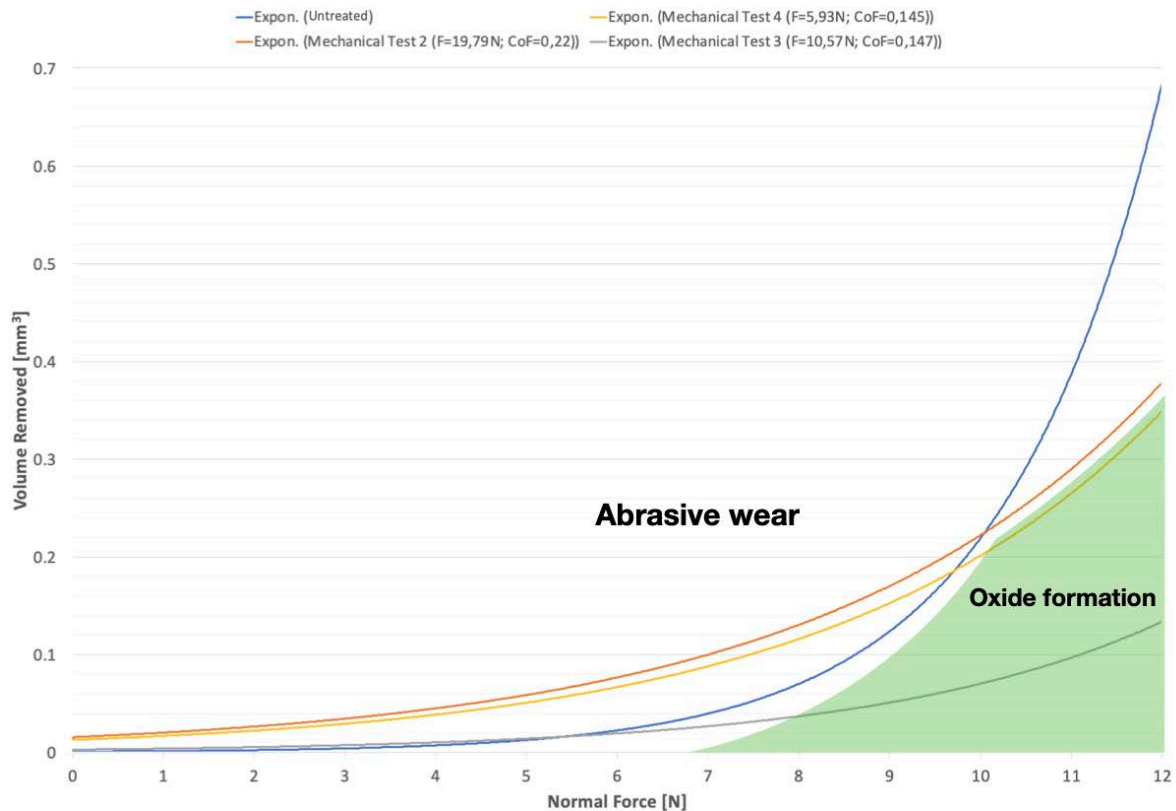
Figure 6.1. Domain of the optimal conditions for the formation and fixation of oxides in the wear marks and consequent improvement of the mechanical properties of the alloy Co28Cr6Mo in green, namely the significant reduction of the volume removed by wear.

Figure 6.1 allows additional conclusions to be drawn and reinforces some conclusions already made, through a different representation of the distinct behaviour of the different specimens:

- The untreated specimen (i.e. not mechanically treated) shows poor wear behaviour compared to the other samples for higher values of normal force applied during tribological testing, for which the volume of material removed increases sharply.
- The specimens from Mechanical Test 2 (associated to a normal force of 19.79 N and coefficient of friction of 0.22) and Mechanical Test 4 (associated to a normal force of 5.93 N and coefficient of friction of 0.145) show slightly divergent evolutions, with better results for the latter. In fact, Mechanical Test 4 presented a greater fixation of a

protective layer of oxides when compared to Mechanical Test 2, so this divergence is justified, coherent with the reasoning of this research work.

- The Mechanical Test 3 sample is visibly the one that reveals the lowest values of volume removed of Co28Cr6Mo by wear, and this difference is increasingly noticeable with increasing normal force applied in the tribological tests. This conclusion had already been drawn, being refocused through this representation. Its greater extension within the domain of oxide formation and attachment on wear surfaces is justified.

Thus, it was possible to determine the conditions closest to those required to minimize the wear of this alloy in its applications, namely in biomedical applications in which there is constant and significant wear. All this research work allowed, ultimately, to determine and validate conditions to increase the longevity of this alloy, Co28Cr6Mo, within the human body, thus reducing the need for surgical maintenance interventions (which reduce the quality of life of patients and subject them to increased risks).

6.1. Suggestions for future work

Scientific research usually leaves open doors to further progress. Experimental research may start with incomplete knowledge of the most appropriate settings which are improved as knowledge is acquired during the process. Thus, either trajectory corrections or adjustments in parameters may arise as necessary for fine tuning the procedure. This may even demand restarting parts of the work or even all the experiments. In our case the optimal conditions to obtain results were unknown; thus, it was assumed a very high probability of adjustments necessity, as results during the progress were obtained and analysed. As such, and through a continuous analysis of the results obtained throughout this research, possible improvements were identified that could be carried out in future work. Thus, future work that can be pursued may include:

- The stress-strain curve associated with the alloy in question, Co28Cr6Mo, was obtained from the literature reviewed and is unlikely to correspond to a good approximation. It is proposed that tensile tests be carried out for the material that was tested.
- As mentioned, the numerical simulation as well as the hardness profile do not have enough resolution to highlight the area of the tested Co28Cr6Mo specimens that was affected by the hardening. A modeling with a more refined mesh should be used. Alternative techniques to verify the hardening region, namely the evaluation of residual stresses, should also be considered.

7. REFERENCES

Balagna, C., S. Spriano, and M.G. Faga (2012), 'Characterization of Co–Cr–Mo alloys after a thermal treatment for high wear resistance', *Materials Science and Engineering: C*, 32 (7), 1868-1877.

Blau, P. J. (2009). *Friction Science and Technology from Concepts to Applications*, CRC Press, 2nd Edition.

Casabán Julián, Leandre and Anna Igual Muñoz (2011), 'Influence of microstructure of HC CoCrMo biomedical alloys on the corrosion and wear behaviour in simulated body fluids', *Tribology International*, 44 (3), 318-329.

Chen, Y, et al. (2017), 'Effects of carbon addition on wear mechanisms of CoCrMo metal-on-metal hip joint bearings', *Mater Sci Eng C Mater Biol Appl*, 76, 997-1004.

Clemow, AJT and BL Daniell (1980), 'The influence of microstructure on the adhesive wear resistance of a CoCrMo alloy', *Wear*, 61 (2), 219-231.

Díaz, C., et al. (2014), 'Reduction of corrosion current of CoCr alloys by post-PIII oxidation', *Surface and Coatings Technology*, 256, 59-63.

Dorner-Reisel, Annett, et al. (2004), 'Electrochemical corrosion behaviour of uncoated and DLC coated medical grade Co28Cr6Mo', *Surface and Coatings Technology*, 177-178, 830-837.

Fleming, Thomas J., Alan Kavanagh, and Greg Duggan (2020), 'The effect of melt temperature on the mechanical properties of cast ASTM F75 CoCrMo alloy as explained by nitrogen and oxygen content', *Journal of Materials Research and Technology*, 9 (5), 9479-9486.

García, J. A., Díaz, C., Mändl, S., Lutz, J., Martínez, R., & Rodríguez, R. J. (2010). Tribological improvements of plasma immersion implanted CoCr alloys. *Surface and Coatings Technology*, 204(18-19), 2928-2932.

Henriques, B., et al. (2014), 'Mechanical and thermal properties of hot pressed CoCrMo–porcelain composites developed for prosthetic dentistry', *Journal of the Mechanical Behavior of Biomedical Materials*, 30, 103-110.

Henriques, B., et al. (2015), 'Mechanical properties of hot pressed CoCrMo alloy compacts for biomedical applications', *Materials & Design*, 83, 829-34.

Herranz, G, et al. (2020), 'Mechanical performance, corrosion and tribological evaluation of a Co-Cr-Mo alloy processed by MIM for biomedical applications', *J Mech Behav Biomed Mater*, 105, 103706.

Li, Haoqing, et al. (2020), 'Microstructural features of biomedical cobalt–chromium–molybdenum (CoCrMo) alloy from powder bed fusion to aging heat treatment', *Journal of Materials Science & Technology*, 45, 146-56.

Liao, Y, et al. (2013), 'CoCrMo metal-on-metal hip replacements', *Physical Chemistry Chemical Physics*, 15 (3), 746-56.

Chauhan, M. (2017). *Microstructural characterization of cobalt chromium (ASTM F75) cubes produced by EBM technique*. Unpublished MSc, Chalmers University of Technology.

Mathew, M.T., et al. (2011), 'Tribocorrosion behavior of CoCrMo alloy for hip prosthesis as a function of loads: A comparison between two testing systems', *Wear*, 271 (9-10), 1210-19.

Mischler, Stefano and Anna Igual Muñoz (2013), 'Wear of CoCrMo alloys used in metal-on-metal hip joints: A tribocorrosion appraisal', *Wear*, 297 (1-2), 1081-94.

Mori, Manami, et al. (2012), 'Microstructures and Mechanical Properties of Biomedical Co-29Cr-6Mo-0.14N Alloys Processed by Hot Rolling', *Metallurgical and Materials Transactions A*, 43 (9), 3108-19.

Mróz, A., Garbiec, D., Jakubowicz, J., Łapaj, Ł., Wielowiejska-Giertug, A., & Gierzyńska-Dolna, M. (2016). Effect of manufacturing technology on tribological properties of Co28Cr6Mo alloy. *Inżynieria Materiałowa*, 1(5), 39-45.

Mróz, A., Garbiec, D., Jakubowicz, J., & Łapaj, Ł. (2017). Effect of manufacturing technology of ball-and-socket joint made of Co28Cr6Mo alloy on its tribological properties. *Inżynieria Materiałowa*, 1, 28-33.

Patel, Bhairav, et al. (2012), 'Cobalt-based orthopaedic alloys: Relationship between forming route, microstructure and tribological performance', *Materials Science and Engineering: C*, 32 (5), 1222-29.

Popov, VL (2010), *Contact Mechanics and Friction - Physical Principles and Applications*, Springer, Berlin, Heidelberg.

Ramalho, A. (2004), 'Micro-scale abrasive wear test of thin coated cylindrical surfaces', *Tribology Letters*, 16, 133-141.

Ramalho, A. (2010), 'A reliability model for friction and wear experimental data', *Wear*, 269 (3-4), 213-23.

Razavi, Seyed Mohammad Javad, et al. (2021), 'Effect of heat treatment on fatigue behavior of as-built notched Co-Cr-Mo parts produced by Selective Laser Melting', *International Journal of Fatigue*, 142, 105926.

Reséndiz-Calderón, C.D., et al. (2020), 'Wear and friction of boride layer in CoCrMo alloy under different micro-abrasion modes (rolling and grooving abrasion)', *Materials Letters*, 279, 128500.

Ryu, Jae Joong and Pranav Shrotriya (2013), 'Influence of roughness on surface instability of medical grade cobalt–chromium alloy (CoCrMo) during contact corrosion–fatigue', *Applied Surface Science*, 273, 536-41.

Sadiq, K, MM Stack, and RA Black (2015), 'Wear mapping of CoCrMo alloy in simulated bio-tribocorrosion conditions of a hip prosthesis bearing in calf serum solution', *Materials Science and Engineering: C Materials for Biological Applications*, 49, 452-62.

Seki, Erina, et al. (2019), 'Effect of heat treatment on the microstructure and fatigue strength of CoCrMo alloys fabricated by selective laser melting', *Materials Letters*, 245, 53-56.

Silva-Álvarez, D.F., et al. (2020), 'Improving the surface integrity of the CoCrMo alloy by the ball burnishing technique', *Journal of Materials Research and Technology*, 9 (4), 7592-601.

Stachowiak, G., & Batchelor, A. W. (2014). *Engineering Tribology*. Butterworth-Heinemann, 4th Edition.

Sun, D., et al. (2009), 'Microabrasion–corrosion of cast CoCrMo alloy in simulated body fluids', *Tribology International*, 42 (1), 99-110.

Toh, WQ, et al. (2017), 'Tribochemical Characterization and Tribocorrosive Behavior of

CoCrMo Alloys: A Review', *Materials (Basel)*, 11 (1).

Tonelli, Lavinia, Alessandro Fortunato, and Lorella Ceschini (2020), 'CoCr alloy processed by Selective Laser Melting (SLM): effect of Laser Energy Density on microstructure, surface morphology, and hardness', *Journal of Manufacturing Processes*, 52, 106-19.

Vicente, N., F. Casarib, F., Bucciottic, L., Facchinic, L., & Molinaria, A. (2011). Microstructure and Tensile Properties of Co-28Cr-6Mo Alloy Produced by Spark Plasma Sintering. Proceedings from *Euro PM2011 – PM Biomaterials*, Barcelona.

Vilhena, Luís, Gifty Oppong, and Amílcar Ramalho (2019), 'Tribocorrosion of different biomaterials under reciprocating sliding conditions in artificial saliva', *Lubrication Science*, 31 (8), 364-80.

Wang, SP and J Xu (2017), 'TiZrNbTaMo high-entropy alloy designed for orthopedic implants: As-cast microstructure and mechanical properties', *Materials Science and Engineering: C Materials for Biological Applications*, 73, 80-89.

Yan, Yu, et al. (2006), 'Tribocorrosion in implants—assessing high carbon and low carbon Co–Cr–Mo alloys by in situ electrochemical measurements', *Tribology International*, 39 (12), 1509-17.

Yoneyama, Choshun, et al. (2020), 'Influence of Bovine Serum Albumin (BSA) on the Tribocorrosion Behaviour of a Low Carbon CoCrMo Alloy in Simulated Body Fluids', *Lubricants*, 8 (5), 61.

Zai, W., M.H. Wong, and H.C. Man (2019), 'Improving the wear and corrosion resistance of CoCrMo-UHMWPE articulating surfaces in the presence of an electrolyte', *Applied Surface Science*, 464, 404-11.

Zhang, Mingkang, et al. (2018), 'An investigation into the aging behavior of CoCrMo alloys fabricated by selective laser melting', *Journal of Alloys and Compounds*, 750, 878-86.